ABSTRACT

Title of Dissertation:	Mid-Infrared Laser Driven Avalanche Ionization and Low Frequency Radiation Generation
	Robert Max Schwartz, Doctor of Philosophy, 2022
Dissertation directed by:	Professor Howard Milchberg, Department of Physics

In this dissertation, we discuss the applications of intense mid-infrared laser interactions in three main topics. First, we demonstrate and discuss the remote detection of radioactive materials using avalanche breakdowns driven by picosecond, mid-infrared laser pulses. In the presence of radioactive materials, an enhanced population of free electrons and weakly bound ions are created in air. Laser driven avalanche ionization is a powerful tool for amplifying and detecting this weak signature, allowing for detection at standoff distances beyond the stopping distance of the radioactive particles. This technique can be applied more generally to the detection of any low density plasma. In the second section, we apply a similar method to measure laser ionization yields in atmospheric pressure gas across an extremely wide range. Finally, we demonstrate and discuss the generation of THz and low harmonics from two-color mid-infrared laser pulses. This technique allows for the generation of highly efficient, ultra-broadband coherent radiation.

MID-INFRARED LASER DRIVEN AVALANCHE IONIZATION AND LOW FREQUENCY GENERATION

by

Robert Max Schwartz

Dissertation submitted to the Faculty of the Graduate School of the
University of Maryland, College Park, in partial fulfillment
of the requirements for the degree of
Doctor of Philosophy
2022

Advisory Committee:
Professor Howard Milchberg, Chair
Professor Phillip Sprangle
Professor Brian Beaudoin
Professor Timothy Koeth
Professor Ki-Yong Kim

Table of Contents

List of Figures

Chapter 1: Laser Driven Ionization

1.1 Introduction to Avalanche Breakdowns

Avalanche ionization was the first observed laser driven breakdown mechanism. In early experiments [3,4], q-switched ruby lasers were focused into partially evacuated gas cells and the resultant ionization could be measured through their fluorescence or charged plates. With photon energies around 1.8eV, significantly lower than the ionization energies of air molecules ε_{ion}>10 eV, simple single photon ionization was not able to explain the breakdowns. Theoretical explanations [5] quickly followed describing the process in two parts. First, nonlinear multiphoton ionization can create an initial population of seed electrons. Then, avalanche ionization can exponentially drive that low population into a large, easily detectable plasma.

Following significant earlier work with DC and microwave breakdowns [6–8], a theory of laser driven avalanche ionization was developed [9]. In this process, free electrons are driven by an oscillatory field and experience collisions with nearby neutral atoms. This mechanism, inverse bremsstrahlung, rapidly heats free electrons beyond the ionization potential of nearby neutrals, at which point they can drive collisional ionization. The proceeding exponential cascade in which a single free electron frees another, then both electrons free two more, quickly grows few free electrons into a large, observable plasma.

While avalanche ionization provides an adequate description for the growth of plasma driven by q-switched lasers, it relies on the presence of an initial population of free electrons to seed the process. Background radiation from cosmic rays and terrestrial sources creates a steady state free charge density of around $10^3/cm^3$ [10]. For a tightly focused beam, this may lead to zero expected free charges near the laser focus to seed the breakdown. Instead, a theory of multi-photon

and tunnel ionization was developed in which multiple photons from an intense laser field can ionize an atom [11–13].

1.2 Classic Theory of Avalanche Breakdowns

We can consider the simple case for a long pulse laser source interacting with a neutral gas containing one free electron. For a linearly polarized laser field $E = E_0 \sin \omega t$ a free electron will oscillate with the field with velocity

$$v = \frac{eE_0}{m_e \omega} \cos(\omega t)$$

The electron will have mean quiver energy $U_P = e^2 E_0^2 / 4 m_e \omega^2$. If the energy is greater than the ionization energy of the surrounding gas, this electron could immediately collisionally ionize the neutrals. Otherwise, repeated elastic collisions dephase the electron velocity from the driving laser field, transferring energy from the quivering motion to random motion. The time averaged heating rate is

$$\frac{d\varepsilon_e}{dt} = \frac{e^2 E_0^2}{2 m_e \omega^2} \nu_e \frac{\omega^2}{\omega^2 + \nu_e^2}$$

where ν_e is the effective collision rate between electrons and surrounding neutrals and ions. For electrons with energies between 1-50eV in air at atmospheric pressure, the collision rate $\nu_e \sim 2 - 4$ ps^{-1} [14] is significantly lower than optical frequencies, so the heating rate can be simplified

$$\frac{d\varepsilon_e}{dt} \approx \frac{e^2 E_0^2}{2 m_e \omega^2} \nu_e = 2 U_p \nu_e \propto I \lambda^2$$

Once an electron is heated to energies above the ionization potential ε_{ion}, inelastic collisions can liberate new electrons which are then further heated by the laser field. Each ionization generation doubles the total number of free electrons and takes an average time $\Delta t =$

$\frac{\varepsilon_{ion}}{2U_p\nu_e}$. The exponential growth can continue until saturation when the initial neutral population is fully ionized. So in this simple model, we can define the minimum threshold for a laser of pulse length τ_p to drive an avalanche N generations

$$I_{th} = \frac{N\varepsilon_{ion}c^3\epsilon_0 m_e}{4\pi^2\tau_p e^2\nu_e}\frac{1}{\lambda^2}$$

The inverse squared wavelength scaling allows longer wavelength lasers to drive avalanche at lower intensities. Note that this threshold ignores all loss mechanisms. A more complete model [15] tracks the electron temperature and losses due to ionization, vibrational and rotational excitation of molecules and other inelastic processes. The temperature grows according to

$$\frac{\partial\varepsilon_e}{\partial t} = 2U_p\nu_e - \dot{\varepsilon}_{loss} - \nu_{ion}\varepsilon_e$$

Where $\dot{\varepsilon}_{loss}$ is the electron energy loss rate and ν_{ion} is the temperature dependent net ionization rate. Using the constants from [16] the ionization rate crosses zero at approximately 1.5eV, leading to a breakdown threshold (where the steady-state temperature is 1.5eV) for a 3.9 μm laser to be 0.25 TW/cm^2.

This result can be compared to an earlier model [17,18] which considers losses only through electronic excitement of nitrogen. This model finds a breakdown threshold in air to drive a plasma from 10^5 /cm^3 to 10^{18} /cm^3 to be

$$I_{th} = \frac{800}{\tau_p\lambda^2}(1 + 4.5\times10^{-6}\lambda^2)(1 + 2\times10^8\tau_p)$$

Where I_{th} is in W/cm^2, τ_p is in seconds, and λ is in microns. For a 50 ps, 3.9 μm laser pulse, the breakdown threshold intensity is about 1TW/cm^2. At these long wavelengths and low intensities, the probability of generating seed electrons through multi-photon processes significantly decreases, as discussed in Section 1.3.

1.3 Multiphoton and Tunnel Ionization

When a laser's photon energy is less than the ionization energy of an atom, the typical case for optical frequencies and dielectric materials, single photon linear processes are not sufficient to ionize the atom. Instead, ionization occurs through tunneling or multiphoton ionization. These are two limits of the same process [13], with the transition between them characterized by the Keldysh parameter $\gamma_K = \sqrt{\varepsilon_{ion}/2U_P} \propto 1/\lambda$.

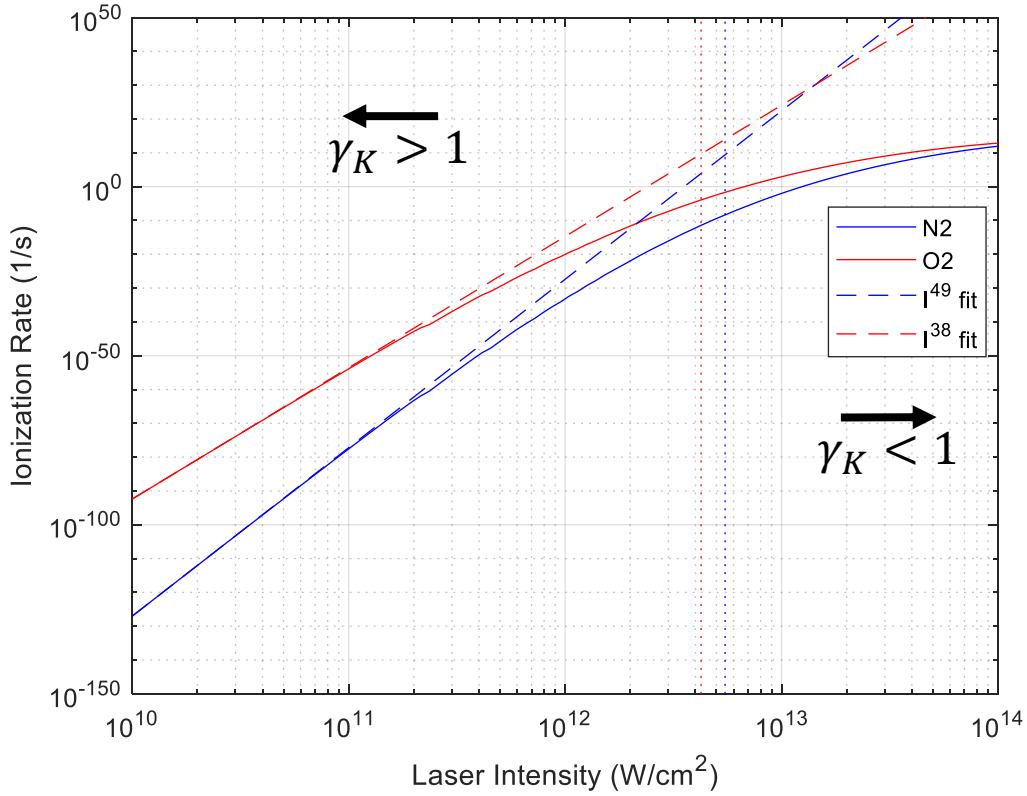

Figure 1.1 Calculated ionization rates for N2 and O2 by a 3.9 μm laser. The dashed lines show a fit to an exponential MPI rate. The blue and red dotted vertical lines show the intensity where the Keldysh parameter is one for N2 and O2 respectively.

For large values of $\gamma_K \gg 1$, multiphoton ionization dominates. In this regime, $N = \text{ceiling}(\varepsilon_{ion}/\varepsilon_{photon})$ photons are required to have enough energy to free an electron. Ionization is increasingly unlikely for large values of N, since the probability of simultaneously absorbing multiple photons is very low. The ionization rate in the MPI regime is $\nu_{MPI} = \sigma(\lambda)I^N$, where $\sigma(\lambda)$ is a wavelength-dependent coefficient.

For small values of $\gamma_K < 1$, tunneling ionization becomes the dominant mechanism. Here, the laser field is strong enough to suppress the Coulomb potential binding an electron to the atom, allowing the electron to tunnel through the reduced effective potential. In this regime, the ionization rate, $\nu_{tunneling} \propto \sigma I^{p<N}$, scales with a reduced dependence on the number of required photons for MPI.

Figure 1.1 shows the calculated ionization rates for molecular nitrogen and oxygen by a 3.9 μm laser using the model described by [19]. The dashed lines show a fit to a simple $\nu_{MPI} \propto I^N$ fit, which follows the complete curve well on the left side where the Keldysh parameter is $\gg 1$. On the right hand side, where the Keldysh parameter is < 1, the slope reduces as ionization enters into the tunneling regime.

We can see from this plot that at 1 TW/cm^2 for a 50 ps, 3.9 μm laser pulse the multiphoton ionization rate for molecular oxygen is only about 1×10^{-20} /s. Even in the most optimistic regime of a square pulse in air comprised solely of oxygen, this would only yield approximately 1×10^{-11}/cm^3 free electrons, significantly lower than the background density.

1.4 Discrete Growth of Avalanche Plasmas

Infrared lasers operating close to the avalanche breakdown threshold in air are not intense enough to drive substantial multiphoton ionization of the neutral medium. The seed electrons must be initially present for the breakdown to occur. Additionally, for short pulse lasers, the breakdowns do not have enough time to diffuse into a smooth, continuous plasma. Instead, each seed electron evolves into a small plasma ball with its radius bounded by the diffusion of hot electrons.

First, we can consider the spatial evolution of a single breakdown. In the simplest case, we can treat the expansion of the plasma as unconstrained diffusion of hot electrons mediated by collisions with surrounding neutrals. An electron at temperature T_e will have an average thermal velocity $v_e = \sqrt{3k_bT_e/m_e}$. With an average electron-neutral collision rate of ν_{en}, an electron will travel approximately $\ell = \sqrt{3k_bT_e/m_e\nu_{en}^2}$ between collisions. For a laser pulse of duration τ_p, the electron will experience $N = \tau_p\nu_{en}$ collisions and will expand to a radius of

$$r_d = \ell\sqrt{N} = \sqrt{\frac{3k_bT_e\tau_p}{m_e\nu_{en}}}$$

At typical values for a near-threshold breakdown in air with 50 ps laser pulse, electron energies $\frac{3}{2}k_bT_e$~10 eV, and ν_{en}~4 ps^{-1}, the diffusion radius is about 4 μm.

As the hot, fast electrons expand about the slower positive ions, charge separation slows the expansion of the plasma. When the diffusion radius approaches the Debye length $\sqrt{\varepsilon_0k_bT_e/ne^2}$, the plasma grows at the lower ambipolar diffusion rate [20,21]. We can thus treat the simple diffusion model as an upper bound on the growth of an avalanche plasma from a single seed.

For a low initial seed density, $\eta_{seed} < 1/r_d^3 \sim 10^{10}\text{cm}^{-3}$ the plasmas that grow out of each seed will remain isolated. An important result of this is that the growth of the plasma is limited to saturation within the diffusion volume of each seed electron rather than the entire focal volume.

1.5 Rate Equations for Short Pulse Infrared Driven Avalanche Breakdown

We can combine our tracking equation for electron temperature, temperature dependent growth rates, and plasma diffusion to evolve a plasma seeded by a single electron. For pulses that are long enough that the electrons have time to thermalize, we can calculate the steady-state temperature as a function of instantaneous laser intensity: $\frac{\partial \varepsilon_e}{\partial t} = 0$. Since the typical electron collision rate $\nu_{en} \approx 2 - 4$ /ps, for pulses of length $\tau_p \gg 1/\nu_{en}$, there will be a large number of thermalizing collisions while the laser intensity is slowly varying. For this temperature, we can also find the temperature dependent ionization rate. Figure 2.2(a) shows steady-state temperatures and ionization rates for a 3.9 μm.

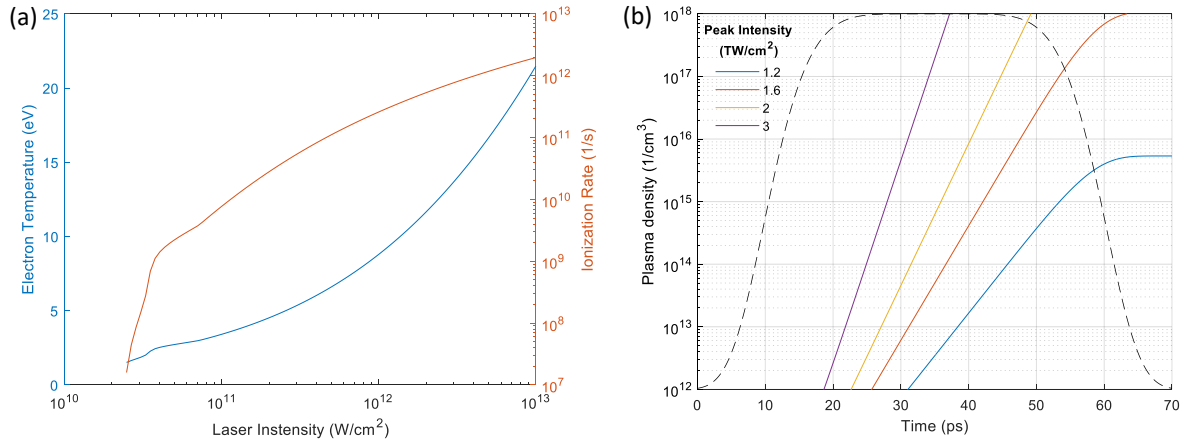

Figure 1.2 (a) Calculated steady-state electron temperatures (blue) and ionization rates (red) for plasmas driven in air with a 3.9 μm laser. **(b)** Calculated avalanche ionization growth driven by a 50 ps, 3.9 μm super-Gaussian laser pulse with various peak intensities. The dashed black line shows the laser envelope.

For a given pulse shape, we then can have the instantaneous electron temperature and ionization rate track with the laser intensity. As discussed in Section 1.2, for intensities below 0.25 TW/cm^2, the temperature is below the threshold needed to overcome losses so avalanche ionization cannot proceed. The temperature and effective ionization rate rise rapidly as the intensity is increased above this threshold.

Coupling this to the diffusion driven growth of the plasma gives us the time evolution of avalanche breakdown seeded by a single electron. For a 50 ps, 3.9 μm laser pulse for various peak intensities, the growth of the plasma is shown in Figure 1.2(b). Our simulations stop when the plasma density reaches 10^{18}/cm^3, at which point the plasma is close to the critical density of the drive laser, 7×10^{19}/cm^3. Near critical density, the plasma efficiently absorbs the energy from the drive laser, rapidly heating and reaching full ionization. We can use this to define a threshold intensity where the laser can drive an avalanche from a single seed electron to a detectable level $I_{th} \approx 1.6$ TW/cm^2.

Chapter 2: Radiation Detection

2.1 Introduction

Remote detection of radioactive materials remains a difficult technical challenge. Direct measurement techniques such as Geiger or scintillation counters rely on radioactive decay products reaching them. These decay products, high energy α-, β-, and γ-particles, fall off with the inverse square of distance, so the probability of detection at range becomes increasingly small. Additionally, attenuation in air further limits the range of α-particles to several centimeters, β-particles to several meters, and γ-particles to several hundred meters Modern state of the art remote detection techniques [22–24] rely on large ($\approx 1 m^2$) scintillator arrays and can detect nuclear materials at a distance up to 100m. Further scaling of these techniques is limited by both the production of ever-larger scintillator arrays and the background noise from cosmic and terrestrial radiation.

Instead, using laser-driven avalanche breakdowns allows a remote source and detector to probe the region immediately surrounding radioactive materials. Nuclear decay products interact with neutral air constituents around them, creating an enhanced population of high energy free electrons. These electrons can further collisionally ionize air molecules. The electrons quickly thermalize then attach to neutral O_2 forming the long-lived but weakly bound O_2^- ion with ionization potential 0.45eV [15,25]. While too low to directly measure, this population can serve as seeds for avalanche breakdown, where the seed density can be determined using several remote diagnostic techniques. As shown in the simulations in Figure 1.2(b), differences in the local laser intensity experienced by a seed electron in air can manifest as clear differences in breakdown rate. By measuring the time it takes to drive a laser-driven avalanche to a detectable level, we can remotely probe the local free charge density created by radioactive materials.

Earlier detection schemes using avalanche ionization proposed using terahertz or millimeter-wave sources to drive breakdowns [26–29], including a proof-of-concept demonstration with a 95 GHz gyrotron used to detect the presence of a 0.64mCi Co-60 source [30]. While the use of longer wavelengths reduces the avalanche breakdown threshold, high power sources in this range are not readily available. The long microsecond pulses generated in these sources makes them susceptible to diffusion of dust and free electrons from background radiation sources into the breakdown volume. Additionally, focusing these sources at long ranges requires extremely large optics to overcome diffraction.

Conversely, high power pulsed lasers in the visible or near-infrared are readily available, such as Nd:YAG and its second harmonic at 1064nm and 532nm and Ti:Sapphire at 800nm. However, for these sources, intensities above the avalanche breakdown threshold will generate large number of free electrons though multiphoton ionization of neutrals, masking the small signal from nuclear materials. In this chapter, we demonstrate the use of a mid-infrared, picosecond laser driver for avalanche breakdown driven radiation detection. Sources in this range do not drive appreciable ionization of neutrals, and the shorter pulses avoid hydrodynamic processes and diffusion into an out of the focal volume that complicate interpretation of the breakdown timing.

2.2 Proof-of-Concept Experiment

2.2.1 Experiment Outline

In this first demonstration experiment [31], we picked off the uncompressed λ=3.9 μm laser pulse after the second amplification stage in the OPCPA where there is a weak residual collinear λ=1.45 μm pulse [32–34]. This allows the use of the strong mid-infrared pulse to drive the avalanche and the weak near-infrared pulse to probe the plasma formation. The experimental

outline is shown in Figure 2.1. Both pulses are focused with a lens (L1) between *f*/10 and *f*/25 towards a 5mCi 18mm Po-210 foil source emitting 4.7 MeV alpha particles. The source is mounted on a stage to adjust its distance to the laser focus and can blocked with an electromechanical shutter. The majority (>99%) of the λ=1.45 μm beam is picked off by a beamsplitter (BS1) onto a PbSe photodetector (PD1). Since the parametric amplification produces directly proportional signal and idler beams, a measurement of the signal pulse also provides a shot-by-shot measurement of the idler energy. The backscattered λ=3.9 μm pump pulse from the plasma is collected at 150° by a second *f*/4 lens (L2) onto a second PbSe photodetector (PD2). The transmitted 1.45 μm pulse is reflected by a second beamsplitter (BS2), and focused with a lens (L3) into a fiber-coupled extended InGaAs spectrometer (Spec1, Avantes NIRLine).

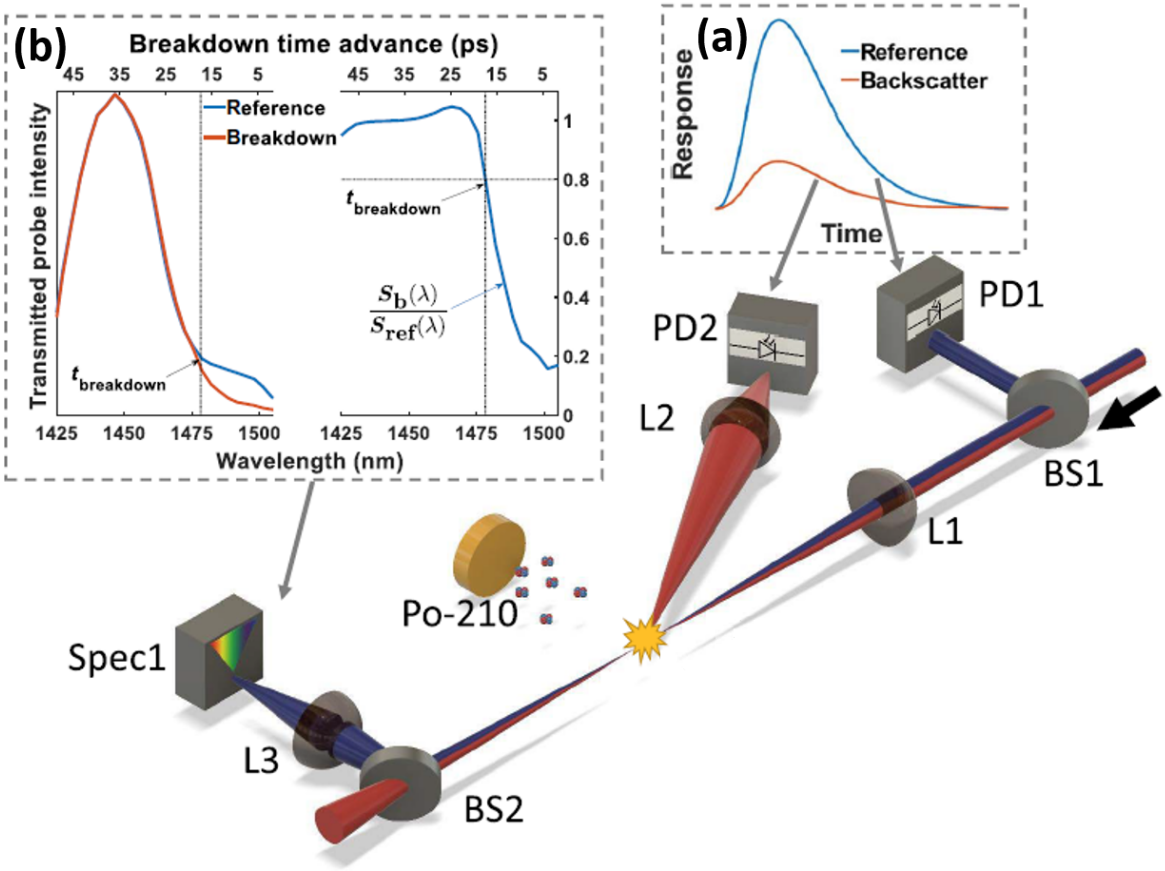

Figure 2.1 Copropagating 50ps FWHM 3.9 μm pump and 1.45 μm probe pulses are generated in an OPCPA. Dichroic beamsplitter BS1 sends most of the probe beam onto PbSe photodetector PD1 for pulse-by-pulse energy measurements. Both beams are focused in the vicinity of a Po-210 α-emitter which creates an enhanced population of free electrons to seed avalanche breakdowns. The backscattered pump pulse is collected by lens L2 onto PbSe photodector PD2. Panel **(a)** shows the two photodetector traces used to determine the relative backscattered pump energy. The forward transmitted probe pulse is separated by beamsplitter BS2 and collected by lens L3 onto near-infrared spectrometer Spec1. Panel **(b)** shows how attenuation of the red size of the probe spectrum is used to determine the breakdown timing, determined by a 20% reduction in signal.

The two breakdown diagnostics are the backscattered pump signal, and the forward transmitted probe spectrum. When the plasma density η_{plasma} approaches the critical density of the laser, the plasma will start to efficiently scatter the laser pulse. As the plasma grows, it

preferentially scatters the later portion of the laser pulse when the plasma density is higher. For the backscattered λ=3.9 μm, the slow photodetector PD2 sees a larger signal when the breakdowns grow faster. We can find the ratio of the pump energy scattered by the plasma by comparing the reference signal on PD1 to the backscattered signal on PD2, shown in Figure 2.1(a). Since the λ=1.45 μm probe is chirped, its attenuation can be measured by the transmitted spectrum. Shown in Figure 2.1(b), when compared to a reference pulse with no breakdown, the probe's breakdown spectrum is attenuated on the red side. By finding the point when the spectrum is attenuated by 20% and mapping the pulse's spectrum to time, we can define the breakdown time advance as the time before the end of the pulse that the breakdown is observed. The mapping of time advance to seed density is discussed further in Section 2.4.2.

2.2.2 On-Off Detection Demonstration

The simplest demonstrations of radiation detection through laser driven avalanche breakdowns shows on-off sensitivity to the presence of a radioactive source. When there is no source present, there are few seed electrons in the air to start the avalanche breakdown. However,

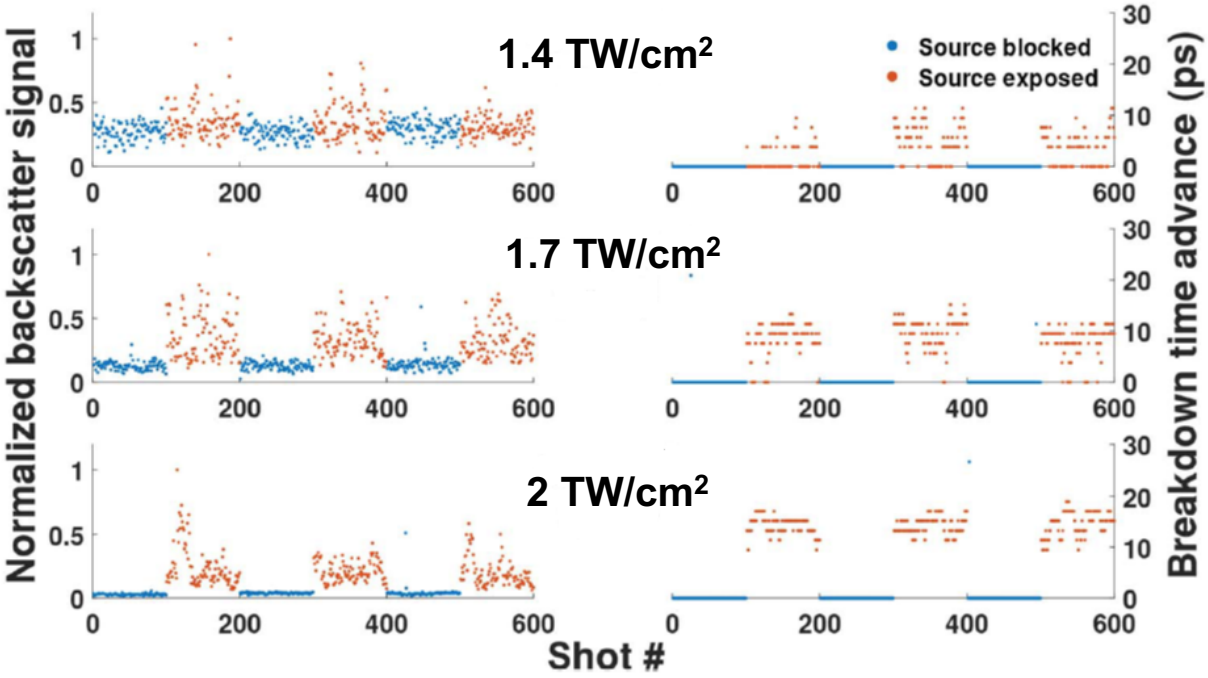

Figure 2.2 A series of shots with the Po-210 source blocked and exposed with an electromechanical shutter every 100 shots. Pump backscatter (left) and breakdown time advance (right) are shown for 1.4, 1.7, and 2 TW/cm^2

when exposed to a radioactive source, the high-energy α-particles generate an enhanced population of free or weakly bound electrons that can seed avalanche ionization. In this regime, breakdowns are only observed in the presence of radiation.

A clear demonstration of the on-off behavior is shown in Figure 2.2. With the α-source 1 cm from the laser focus, we record the backscattered pump and time advance measurements as the source was blocked and unblocked with an electromagnetic shutter every 100 shots. With the exception of random breakdowns likely seeded by dust particles, both diagnostics show a clear distinction between the blocked and exposed Po-210 source. The contrast between blocked and exposed signals substantially increases at higher laser intensities. When the laser driver is stronger, earlier breakdowns are expected, leading to a larger time advance and more backscattered signal.

However, increasing the intensity too much further can degrade contrast due to breakdowns driven by background seed electrons in non-irradiated air, discussed in Section 2.2.3.

2.2.3 Source-Focus Distance Scans

Due to inverse square scaling and absorption in air, the free charge density created by a radioactive source is sensitive to the distance from the source. To measure the free charge density as a function of distance, we scan the Po-210 distance to the focus and record the pump backscatter and probe time advance. Shown in Figure 2.3(a) for *f*/20 focusing, the breakdown time advance increases about 5-10 ps as the source is brought closer to the laser focus, due to an increased free charge density to seed the breakdowns. The steep drop off seen around 3cm is consistent with stopping distance of 3.2 cm for 4.7MeV α-particles [35]. The reduction in breakdown time advance with lower seed density occurs due to the reduced probability of a seed electron being located near the drive laser's peak intensity at the geometric focus.

When the source is sufficiently far from the driver focal volume, lower peak intensities (1.2 and 2.0 TW/cm^2) do not drive the plasma density to saturation, and the probe's spectrum is not significantly attenuated. This produces the zero time-advance points on the plot. Higher peak intensities (2.6 TW/cm^2) can drive breakdowns to saturation even when the source is beyond the α-particle stopping distance. In this case, the region where the laser intensity is greater than the breakdown threshold is large enough to drive avalanche seeded by the significantly lower free charge density. This is seen in Figure 2.3(a) at an intensity of 2.6 TW/cm^2, where breakdowns with a reduced time advance occur at distances greater than 4 cm. At this distance, breakdowns are seeded from the diffusion of O_2^- or other long-lived negative ions beyond the stopping distance of the source. At higher intensities, breakdowns can occur even without a radioactive source present,

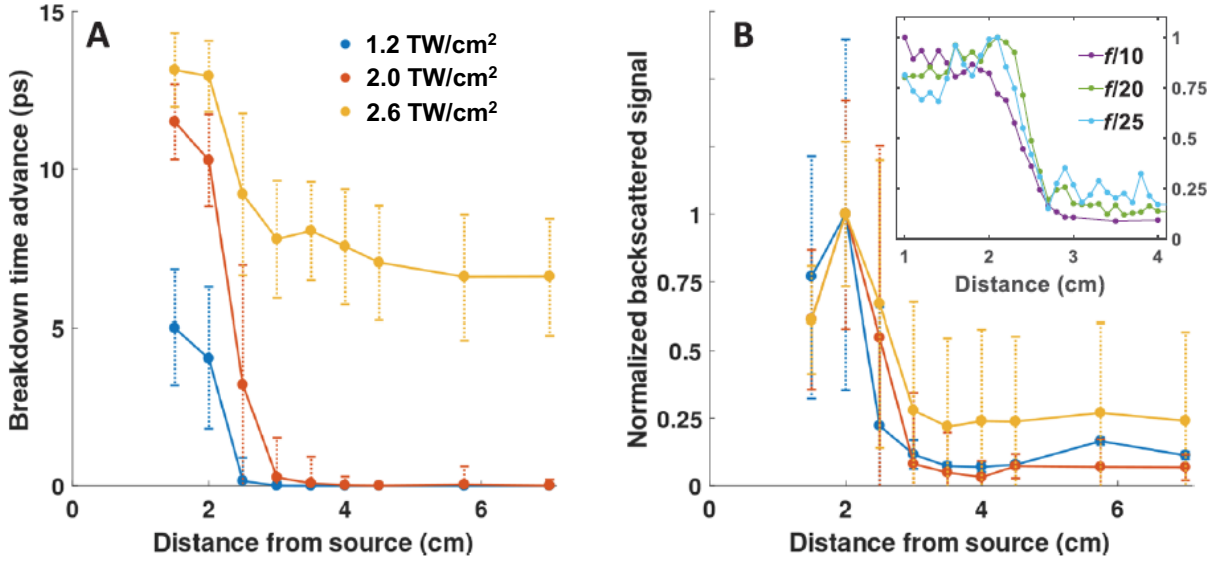

Figure 2.3 Time advance (a) and backscatter signal (b) as a function of source to laser focus distance. For three pump intensities, the source was scanned in distance away from the laser focus reducing the free charge density seeding avalanche ionization. Inset shows backscatter signal for several focusing geometries at a fixed peak intensity of 1.4 TW/cm^2.

with avalanche seeded by the background ion density of ~10^4 cm^{-3} in ambient air, induced by cosmic rays and terrestrial radiation [36].

We simultaneously monitored the backscattering of the pump light from the avalanching plasma. Figure 2.3(b) shows the normalized backscattered signal for the three pump intensities. Similar to the time advance, the backscattered response sees a strong drop off between 2 and 3 cm source to focus distances. At high intensities that induce breakdowns in unseeded air, a large backscatter signal still occurs at distances from the source beyond the α-particle stopping range. At the closest distances with the highest seed densities, the laser drives many breakdowns. The earlier breakdowns can screen the laser from downstream breakdowns, reducing the total

backscattered signal. Since the early breakdowns are still driven quickly, we do not see similar behavior in the time advance measurements.

By varying the focusing geometry, larger or smaller regions can be probed. Longer focal geometries probe larger volumes, enabling sensitivity to lower ion densities. The inset to Figure 2.3(b) shows backscatter measurements for several pump focus geometries at a fixed peak intensity of 1.4 T W/cm^2. The longer *f*/20 and *f*/25 geometries show a drop off in signal at longer source-focus distances and greater response at long distances compared to *f*/10 focusing. By controlling both the peak intensity and the focal geometry, the sensitivity of this technique can be optimized for probing different seed densities. The lower limit for detection sensitivity is determined by the background concentration of free charges.

2.2.4 Comparison to Corona Discharge Seeded Breakdowns and Breakdowns in N_2

To more fully characterize the seed ionization level generated by the 4.7 MeV α-particles from the Po-210 source, we compared the breakdowns of air irradiated by this source to breakdowns seeded by a corona discharge ion generator whose ion production is absolutely calibrated with an ion counter.

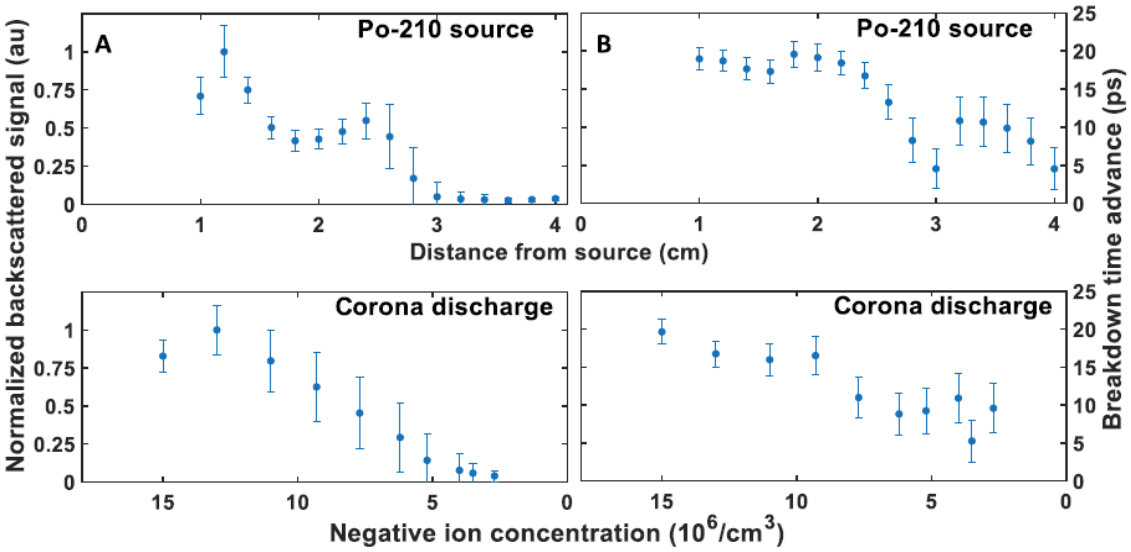

Figure 2.4 Comparison between Po-210 and corona discharge seeded breakdowns. (a) shows the backscattered signal for both Po-210 and corona discharge breakdowns and (b) shows the breakdown time advance. For the corona discharge source, the seed density is labeled based on measurements using a gerdien ion counter.

The corona discharge source (Murata MHM305) maintains a large DC negative voltage between a needle electrode and surrounding ground electrodes, creating a large field gradient around the sharp tip of the needle. The voltage is low enough to avoid arcing between the electrodes, but high enough to drive avalanche ionization of air molecules around the needle electrode. The positive ions are attracted to and neutralized by the needle electrode, and the free electrons travel toward the ground electrode. A small fan placed behind the electrodes blows the free electrons and negative ions towards the laser focus.

We measure the charge density from the corona discharge source with a Gerdien-type ion counter (AlphaLabs AIC2). Gerdien tube ion counters have a tube with a central coaxial electrode. A relatively small voltage is held between the center electrode and the outer wall and a fan blows air through the tube at a known rate. By measuring the current between the outer and inner electrodes and knowing the rate at which air is flowing, the total charge density and polarity of air

can be calculated. Due to the large aperture of the ion counter compared to the rapid gradient in ion density near the Po-210 source, it wasn't possible to directly measure the ion density from the α-source. We note that the background ion density measured by the ion counter far from the radioactive source was ~10^4 cm^{-3}, in agreement with expected negative ion densities in ambient air.

Our results, in Figure 2.4, show comparable breakdowns as measured by breakdown time advance and backscattering, between the two sources when the total negative ion density from the generator is 10^6 to 10^7 cm^{-3}. Comparing to the predicted steady-state negative ion densities predicted by our rate equations discussed in Section 2.4.1, the measured ion densities are somewhat lower. Our model does not include diffusion of long-lived negative ions such as O_2^-, and assumes the negative charge density reaches steady state between subsequent laser pulses (50ms).

We also performed a comparison between breakdowns in air and breakdowns in a pure nitrogen environment. Since N_2^- is not a bound state [37], electrons liberated from neutral nitrogen remain free and do not reattach to form negative ions. The average energy required by an α-particle to create a single ion pair is similar for pure nitrogen and air, about 37 eV and 35 eV, respectively, and the stopping power of both mediums are very similar [35,38]. From this, the total ionization induced by the Po-210 source should be nearly identical in both cases, but in air we expect the charges to mostly consist of O_2^-. We were not able to measure a detectable shift in breakdown timing (within our ~2.5 ps resolution) between air or nitrogen environments when the source is 1 cm from the laser focus. From this we can assume that density of seed electrons is approximately the same in both cases and that any negative ions formed in air are quickly liberated through MPI on the leading edge of the drive pulse

2.3 Single Color Meter-Scale Experiments

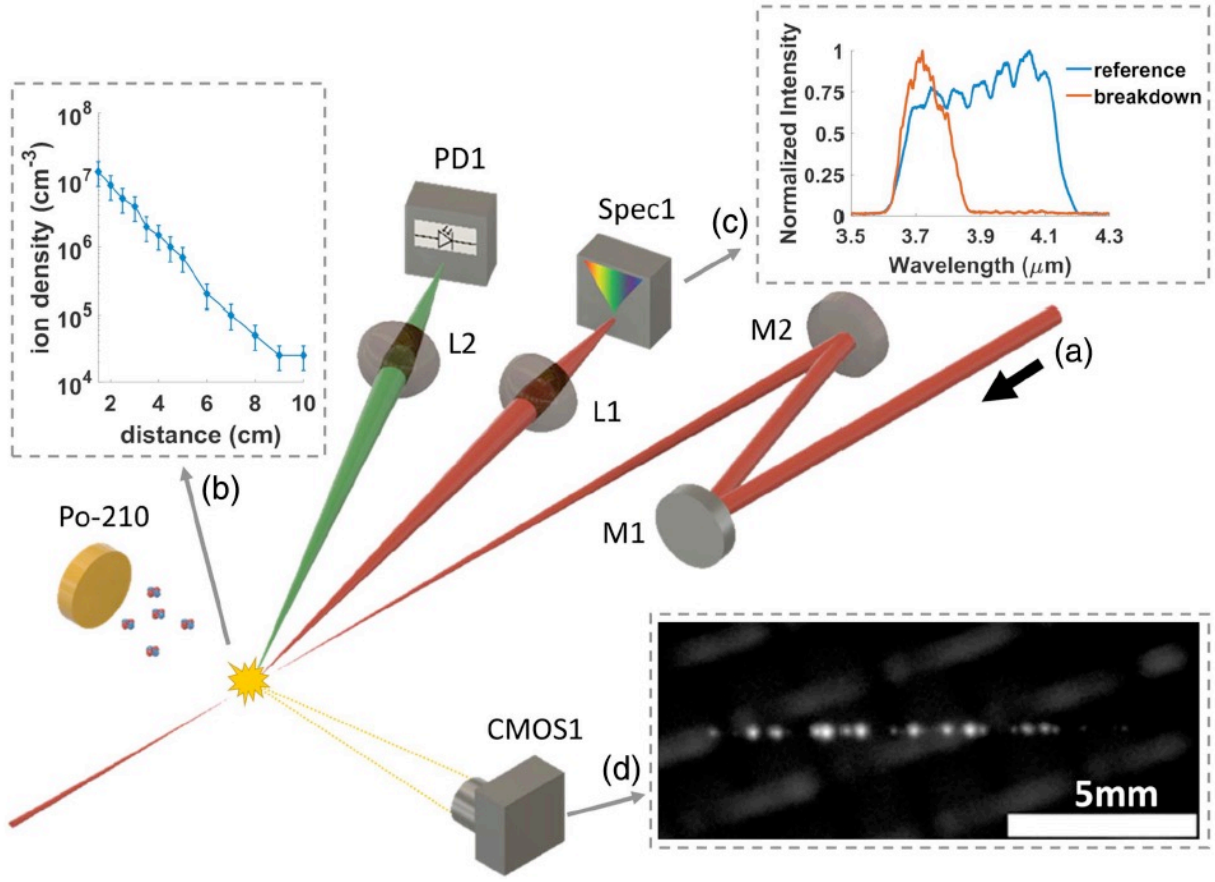

Figure 2.5 **(a)** 15-35mJ 50ps FWHM λ=3.9 μm pump is generated in an OPCPA. The pump is steered by flat mirror M1, and focused at *f*/33 with concave spherical mirror M2. A 5mCi Po-210 α-emitter is mounted on a rail to adjust the distance to the laser focus and behind an electromechanical shutter. The free charge density due to the Po-210 irradiation is plotted as a function of distance in **(b)**. Laser light backscattered by the plasma is collected by lens L1 onto mid-IR spectrometer Spec1. An example breakdown spectrum and the complete laser reference spectrum are shown in **(c)**. Visible plasma emission is captured by lens L2 onto Si photodiode PD1. A low noise camera CMOS1 images the transverse plasma profiles, with an example breakdown plasma shown in **(d)**.

2.3.1 Experimental Outline

Following the proof-of-concept experiment described in Section 2.2, we extended our detection scheme to a 1 meter standoff distance using a spectrally resolved backscatter

diagnostic [39]. The use of only a single color, the chirped λ=3.9 μm pulse, allows the use of all three amplification channels in the OPCPA after which there is no longer a collinear signal at λ=1.45 μm. Using all three channels allows significantly higher pump energies that can drive avalanche breakdowns at a longer range. As an additional benchmark for our standoff diagnostic, a camera imaged the breakdowns, allowing direct counting of individual breakdown sites at very low seed densities down to 10^3 /cm^3.

The experimental layout is shown in Figure 2.5. The amplified, 20 Hz, 15-35 mJ, λ=3.9 μm beam with a 3 cm diameter was generated in the OPCPA (a), bypassing the pulse compressor to create a 50 ps FWHM, super-Gaussian positively-chirped pulse. The pulse was routed with flat mirror M1 and focused at *f*/33 with a 1 m focal length spherical mirror M2. The focused spot size w_0 = 120 μm was measured with an InSb camera. Due to aberrations in the beam, this is larger than expected for a Gaussian beam ($M^2 \sim 1.5$), and the mode changes slightly with the laser energy. Near the laser focus, a 5 mCi Po-210 foil source irradiates the air. The source can be blocked with an electromechanical shutter, and is mounted on a rail to adjust its distance to the laser focus. Increasing the distance decreases the irradiation and number of free charges produced at the laser focus. Figure 2.5(b) shows the measured charge density as a function of distance to the Po-210 source using the Gerdien-tube ion counter. Due to the large aperture and flow through the ion counter, density gradients on the centimeter scale cannot be accurately resolved, but the trend as a function of distance is a reasonable approximation of the Po-210 induced ionization.

The breakdowns were monitored with three standoff diagnostics. First, lens L1 collects the backscattered 3.9 μm pump laser at approximately *f*/80 12° from the laser axis. The light is focused into a single shot mid-IR imaging spectrometer Spec1, comprised of a Horiba MicroHR spectrometer coupled to an LN_2-cooled InSb camera (IRCameras IRC806). Similar to the

transmission spectra from the earlier experiments described in Section 2.2, the backscattered spectrum contains information about the earliest breakdown timing. However, for the transmitted spectrum, the plasma preferentially attenuates later parts of the breakdown where the plasma density is higher. In the backscattered diagnostic, we only see the later parts of the plasma where the pump beam is efficiently scattered towards our detector. A sample reference containing the full laser spectrum and a breakdown spectrum are shown in Figure 2.5(c). In addition to the spectrally resolved backscattered measurement, we also use the total spectrally-integrated backscattered signal as a simple diagnostic of the avalanche breakdowns. Earlier or larger breakdowns scatter a greater portion of the pump beam, leading to a larger integrated signal. A second lens L2, collects the visible (~300-1000nm) plasma emission at *f*/18 16° from the laser axis. This light is collected on an amplified Si photodiode PD1 (Thorlabs PDA100A2). Unlike the backscattered pump, which is sensitive to both the timing and size of breakdowns, this diagnostic is proportional to the total number of ionized electrons in the entire breakdown. Diagnostics were recorded at 10Hz, limited by the data acquisition rate.

As an additional benchmark for the backscatter diagnostics, we also used a low noise camera CMOS1 (Thorlabs Quantalux) to image the transverse plasma profile. Figure 2.5(d) shows a sample image of the breakdowns, with the protective grid covering the Po-210 visible in the background. Each spot in the image shows a single breakdown site.

2.3.2 On-Off Detection Measurements

Following the previous demonstration described in Section 2.2.2, we first show on-off detection in Figure 3.6, with the Po-210 source 2 cm from the laser focus. In these measurements, signals from our breakdown diagnostics were recorded for 1000 consecutive laser shots, with the Po-210 shutter opening or closing every 50 shots. For three intensities: 1.88, 2.25, and 3 TW/cm^2,

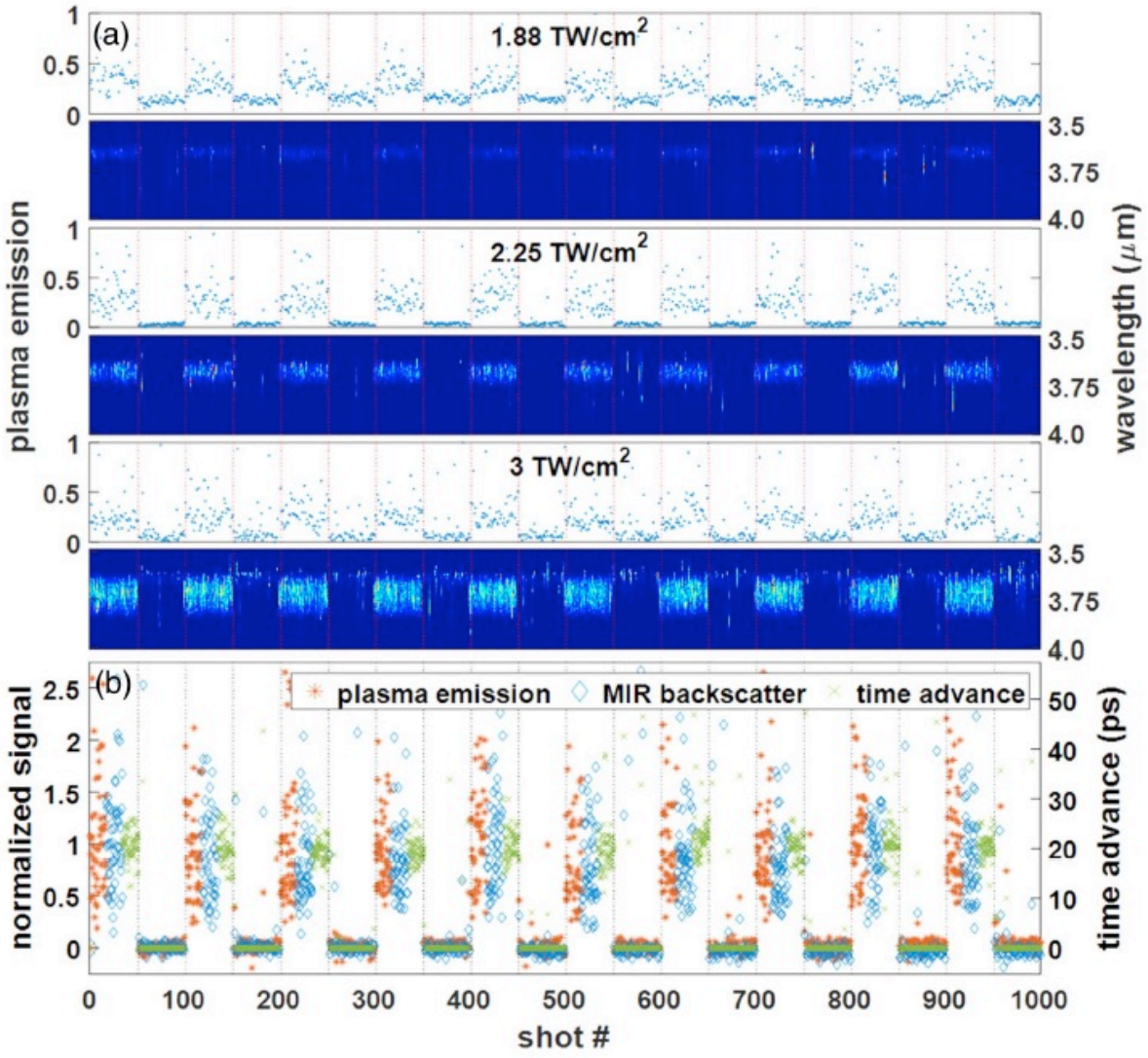

Figure 2.6 Real-time recording of avalanche breakdowns using standoff diagnostics as the Po-210 is blocked and unblocked with an electromechanical shutter every 50 shots. **(a)** Top panels show the visible plasma emission and bottom panels show the backscattered pump spectra for three pump laser peak intensities. **(b)** shows all three diagnostics on a single plot for 2.25 TW/cm^2 peak intensity. Total MIR backscatter is found by integrating the backscattered spectra.

Figure 2.6(a) shows the visible plasma emission (top panels) and the backscattered pump laser spectrum (bottom panels).

As the intensity is increased, the backscattered spectra grows in brightness and spectral width. Higher intensity pump lasers drive faster breakdowns that scatter earlier, redder portions of

the laser. The total brightness of the backscattered signal increases with the energy of the pump laser, how quickly the plasma grows, and the total size of the plasma. At 3 TW/cm^2, breakdowns are observed even in unseeded air, seeded by the background concentration of free charges.

At low intensity, the visible plasma emission has poor contrast between irradiated and non-irradiated air. The breakdowns are small and highly variable leading to a poor signal-to-noise ratio. Conversely, at high intensity, even non-irradiated air produces measureable emission on the visible photodiode. While these breakdowns are significantly weaker than the large, seeded breakdowns, this again reduces the signal-to-noise ratio for this diagnostic. At the middle intensity, 2.25 TW/cm^2, the best contrast is observed in the visible emission. Here, although there is still large variability in the visible emission, the difference between seeded and unseeded breakdowns is clearly observable.

At all intensities, seeded or unseeded, 2-3% of shots show significantly larger than expected signals on all diagnostics. These breakdowns are also observed in the direct imaging diagnostic as a single very bright breakdown. We attribute these anomalously large breakdowns to random seeding by dust or aerosol droplets in the air. Breakdowns from these solid-density targets have ionization thresholds several orders of magnitude lower than for clean air, and create very large, high density plasmas [40].

Figure 2.6(b) shows all three diagnostics for 2.25 TW/cm^2 pump laser intensity on a single plot. For clarity, for the shots where the source is unblocked, we show the diagnostics squeezed into consecutive bins rather than on top of each other. Each diagnostic is normalized by subtracting the median non-irradiated signal, then dividing by the median irradiated signal. The median and not the mean is used to avoid skewing by large dust-seeded breakdowns.

At this intensity, all three diagnostics show a clear on-off behavior as the shutter blocks and unblocks the Po-210 source. The visible emission and pump backscatter measurements exhibited very high shot-to-shot fluctuations, with standard deviations of 42% and 52%, respectively. The time advance shows significantly lower variability, with a standard deviation of 21%.

Both the visible emission and pump backscatter energy diagnostics are sensitive to the random placement of breakdown sites within the focal volume. Variations in the location of seed electrons lead to large differences in the total size and densities of the avalanche plasmas. The forward travelling pump and the backward travelling signals scatter off earlier breakdowns and the signals from each breakdown interfere with each other, further complicating the total measured response on these diagnostics. This effect is discussed in greater detail in Section 2.3.4.

The time advance measurements however, are largely insensitive to these effects. The red edge of the backscattered spectrum is determined by the earliest breakdown, occurring at the location of the seed electron at highest intensity. Since the number of breakdowns in the focal volume is large, there is a high probability that an electron will be randomly positioned very close to the highest intensity region of the laser focus. While the total measured signal includes the spectral content from all the breakdowns that are affected by interference and spectral fringing, the total width of the measured spectrum is largely independent of these effects.

2.3.3 Source-Focus Distance Scans

Similar to the earlier measurements presented in Section 2.2.3, we scanned the α-source-to laser focus separation over 1–9 cm while keeping the peak intensity fixed at 2.25 TW/cm^2. Figure 2.7(a)–(c) shows the raw data from each of the standoff diagnostic and Figure 2.7(d) shows the normalized mean and standard deviation of the measurements.

Shown in Figure 2.7(d), at longer distances, all three diagnostics show very similar response as the source is moved further away. Beyond the stopping distance of a 4.7 MeV α-particle, each diagnostic shows a steady decay as the free-charge density approached the background concentration. At closer distances with significantly higher free charge densities, the total backscattered signal and the visible emission see a sharp drop-off not seen in the time-advance measurement. The high seed density means that an electron is extremely likely to be very close to the region of highest pump intensity, leading to a plateau in time advance.

As described in Section 2.3.2, the large number of breakdown sites leads to scattering and interference between the individual plasmas and suppression of the pump laser by earlier plasmas. This leads to a counter-intuitive *drop* in these diagnostics as the seed density increases. Direct imaging measurements described in Section 2.3.4 shed more light onto this phenomenon.

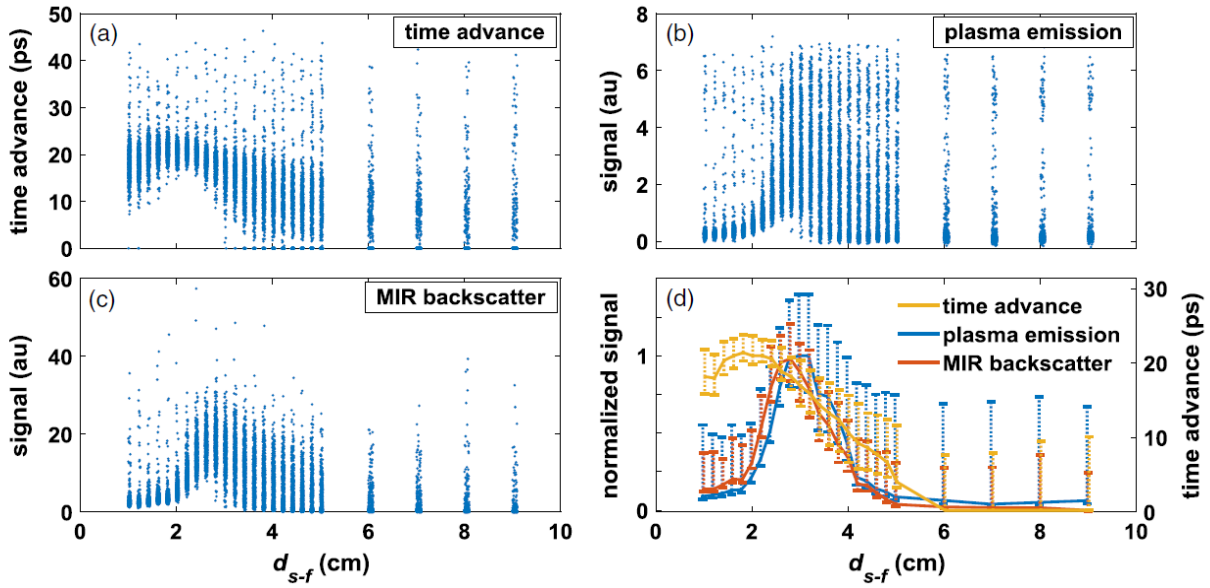

Figure 2.7 Single-shot standoff diagnostic measurements as a function of source to laser focus distance for 2.25 TW/cm^2 peak intensity. Time advance **(a)**, plasma emission **(b)**, and total integrated mid-IR backscatter **(c)** signals are plotted for 1 to 9 cm source to focus distances showing all 500 shots at each position. **(d)** shows the mean value and standard deviation for each diagnostic.

2.3.4 Direct Breakdown Imaging

As discussed in Section 1.4, for all the conditions of our experiments, breakdowns consisted of discrete, countable avalanche sites. Through direct imaging of the transverse plasma profile, individual seed ion locations in the focal volume can be directly counted (see example image in Figure 3.5(d)). This absolute measurement of the number of breakdown sites allows for verification and calibration of our standoff diagnostics. For each image, the number of breakdowns and the FWHM of the breakdown plasmas were extracted. For peak laser intensities between 1.5 and 3 TW/cm^2, Figure 2.8 shows (a) the number of breakdowns sites and (b) the FWHM of the largest observed breakdown, averaged over 500 shots, as a function of the distance between the Po-210 source and the laser focus. While the gerdien-tube ion counter cannot accurately resolve centimeter-scale features, ion density measurements are rescaled and overlaid for reference.

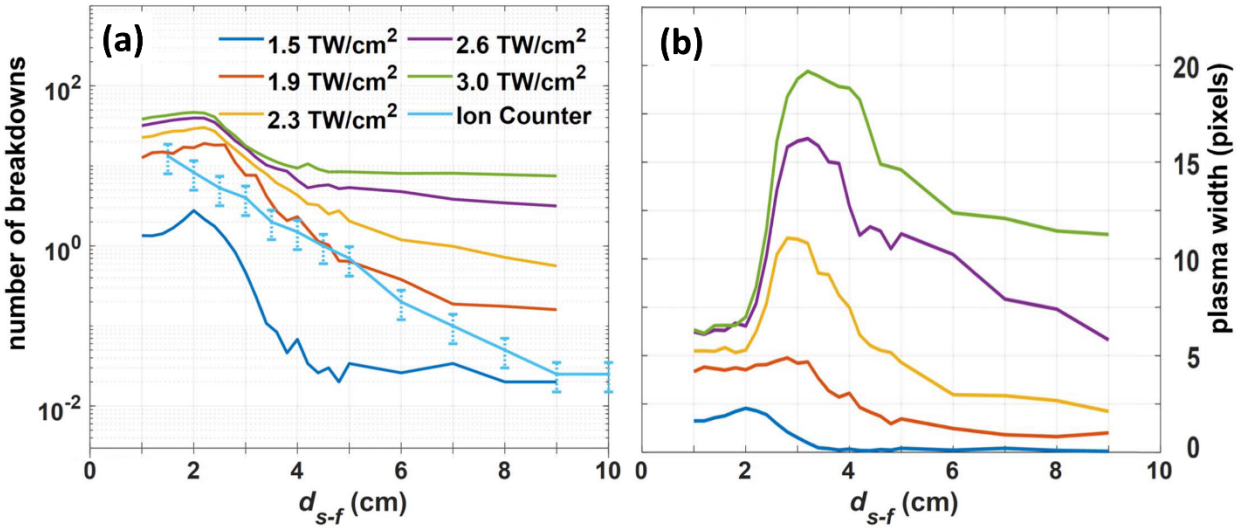

Figure 2.8 Direct transverse imaging of the visible emission from breakdown plasmas (example shown in Figure 2.5(d)). **(a)** shows the mean number of breakdowns for 500 shots for a range of laser intensities and source to focus distances. The ion counter measurements rescaled and plotted as a scaling comparison. **(b)** shows the mean value of the largest breakdown width in each shot. The spatial calibration is approximately 50 μm per pixel.

To correlate the total breakdown counts to a seed density, we must consider the volume within which the laser intensity I is above the breakdown threshold I_{th}, described in Sections 1.2 and 1.5. For a Gaussian beam focused to a spot size w_0, the total focal volume for which I is greater than I_{th} is given by [27].

$$V_{th} = \frac{\pi^2}{3}\frac{w_0^4}{\lambda}\left\{\frac{2}{3}\left(5+\frac{I}{I_{th}}\right)\sqrt{\frac{I}{I_{th}}-1} - 4\tan^{-1}\left(\frac{I}{I_{th}}-1\right)\right\}$$

The number of observed breakdowns sites is the product of the seed density and focal volume. Increasing either the seed density or the peak laser intensity will increase the number of breakdowns observed. Shown in Figure 2.8(a), we can see that more counts are measured for both higher laser intensities and closer source to laser focus distances. For a given source distance, we can fit the number of observed breakdowns to V_{th}, using I_{th} as the fitting parameter. For distances between 1 and 4 cm, we calculate the threshold intensity to be between 0.9-1.3 TW/cm^2. While higher than the minimum intensity needed to overcome losses (≈0.25 TW/cm^2), this threshold is somewhat lower than the intensity required for our backscatter diagnostics (≈1.6 TW/cm^2). Since the plasma does not need to reach saturation to be detectable through visible emission, the side imaging diagnostic is more sensitive than backscattered diagnostics.

Due to the low resolution of our imaging system (~50 μm), at high seed densities multiple breakdown sites can overlap and only be counted as one. Additionally, at high seed densities, the scattering and refraction from earlier plasmas can screen the drive laser downstream, further suppressing the number of breakdowns. Both of these effects can lead to an undercounting of total breakdowns, an overestimate of the focal volume, and an underestimate of the threshold intensity.

The plots in Figure 2.8(a) show the breakdown counts as a function of source to focus distance. For intensities between 1.5 and 3 TW/cm^2 focused to spot size w_0 = 120 μm, the focal

volume above threshold V_{th} ranges between 2.7×10^{-5} and 2.7×10^{-4} cm^{-3}. Dividing the observed breakdown sites by the probed volume gives a peak seed density of around 10^5 cm^{-3} for 2.5 cm source to focus distance and 10^4 cm^{-3} for a 4 cm distance. While the breakdown counts roughly track with our ion counter measurements, the observed breakdown counts are about two orders of magnitude lower. The location of the peak density corresponds to the Bragg peak for a 4.7 MeV α-particles in air [35]. The Bragg peak occurs just prior to the end of the α-particle's 3.2 cm range, when the stopping power significantly as the particle loses energy to interactions with air molecules.

Beyond this distance, the observed breakdown counts rapidly drop. Seed electrons here do not come directly from interactions between α-particles and air, but rather through diffusion or other secondary processes from interactions closer to the source. At longer distances, even accounting for the intensity-dependent focal volume, the calculated seed densities are intensity dependent. The increase in seed density scales roughly as $\eta_{seed} \propto I^{4-5}$. The exponent term is highly sensitive to the threshold intensity. If, as described earlier, the threshold intensity is underestimated, the exponent will be larger.

The I^N dependence of the seed density scales similarly to multiphoton ionization, implying that a possible explanation for this behavior is a population of molecules with binding energies above O_2^- (0.45 eV), but below major neutral air constituents (10-15 eV). While O_2^- is long-lived, further interactions in air lead to a complex reaction chain generating more stable, higher ionization potential negative ions. In α-irradiated air, numerous ions are created including O^-, OH^-, O_3^-, CO_4^-, NO_2^-, NO_3^-, HCO_3^-, as well as their hydrates [41,42]. With ionization potentials of 2-5 eV [37], these will be preferentially ionized for higher intensity drive lasers, and are more likely to be ionized later in the pulse, where the avalanche breakdowns may not be detectable on the time

advance diagnostics. Another possibility, discussed in Chapter 3, is the ubiquitous presence in air of a contaminant with an ionization potential of approximately 6 eV at a relative concentration of 10^{-9} to 10^{-11} [43].

In addition to the total number of breakdowns, we also measured the FWHM of the largest breakdown in each frame, shown in Figure 2.8(b) where each pixel represents about a 50 μm plasma width. The largest and brightest breakdowns correspond to plasmas that absorb and then scatter the greatest amount of laser energy. For intensities greater than 1.9 TW/cm^2, the maximum plasma widths are seen at a distance of around 3 cm, further than the distance where the maximum breakdown counts are observed. At closer distances, the maximum plasma size rapidly decreases and clamps to around 5 pixels (250 μm). For 1.9 TW/cm^2 peak intensity, the peak plasma size still occurs near 3 cm source to focus distance, but the decrease at closer separations is significantly reduced. Similarly, for 1.5 TW/cm^2, the peak occurs at 2 cm, with only a small decrease at closer distances.

From Figure 2.8(a), we can see that the peak plasma size is not directly proportional to the number of breakdowns, since the peak plasma size does not typically occur when the highest number of breakdowns are observed. Therefore, it is not simply a product of a seed electron being closest to the geometric focus where the peak laser intensity occurs. For sufficiently high seed densities, scattering, refraction, and absorption from multiple breakdown plasmas can significantly impact the propagation of the drive laser.

Mie scattering from upstream breakdowns reduces the intensity of the laser, limiting the heating and growth of downstream breakdowns. For a simple model that will overestimate this effect, we treat the breakdown plasma as a 250 μm diameter sphere, based on the peak width of the clamped plasmas as shown in Figure 2.8(b). If the breakdown occurs close to the focus, it will

occlude half the longitudinal extend of the focal volume, about 3mm. This corresponds to an occluded volume of about 10^{-4} cm^3 per breakdown. Thus, for seed densities greater than 10^4 cm^{-3}, the breakdowns will be spaced close enough that scattering from upstream plasmas will clamp the heating of downstream breakdowns.

This effect is also seen in Figures 2.3(b) and 2.7, where the visible emission and total backscattered 3.9 μm signal are strongly reduced when the source is close to the laser focus and the seed density is highest. Since plasmas will only be sufficiently large and high density to significantly affect the propagation of the laser towards the end of their evolution, we do not see this effect in the time advance measurements. The time advance is determined by the breakdowns that are driven the fastest, which necessarily will not experience any effects from later plasmas, while the visible emission and total backscattered signal sample all the breakdowns throughout the entire pulse.

A complete analysis of this phenomenon would require a 3D treatment of the time-dependent development of randomly distributed breakdown sites. While this is beyond the scope of this work, laser driven plasma clamping in the avalanche regime has been observed in prior work. Experiments creating dense plasma channels using a femtosecond filament pre-ionizing pulse and a nanosecond heater pulse found that the resulting plasma was fragmented due to the shielding of earlier plasmas [44]. The use of avalanche ionization for making continuous laser driven plasma channels [45] requires the use of either significantly more energy, or non-spherical focusing optics to avoid the discontinuities caused by the shielding between individual breakdown sites. In a direct measurement of this effect [46], breakdowns in carbon black suspensions showed that nonlinear plasma scattering significantly clamped the transmission of a nanosecond laser pulse.

2.4 Discussion

2.4.1 Free Charge Density from Radioactive Materials

Free electrons in air rapidly attach to neutral molecular oxygen, forming O_2^- ions, and later, a cascade of further negative ion species. Although accounting for the full air chemistry quickly becomes intractable, we can use a simplified model that tracks the populations of free electrons and O_2^- ions and the temperature of electrons [16]:

$$\frac{\partial \eta_e}{\partial t} = \nu_{rad} + \nu_{photo}\eta_- + \nu_{coll}\eta_e - \nu_a\eta_e + \beta_{e+}\eta_+\eta_e + \beta_n\eta_n\eta_-$$

$$\frac{\partial \eta_-}{\partial t} = -\nu_{photo}\eta_- + \nu_a\eta_e - \beta_{\pm}\eta_+\eta_- - \beta_n\eta_n\eta_-$$

$$\frac{3}{2}\frac{\partial(\eta_e T_e)}{\partial t} = 2U_p\nu_e\eta_e - \eta_e\dot{\varepsilon}_{loss}$$

Here we have $\eta_e, \eta_-, \eta_+,$ and η_n, the number densities for free electrons, negative ions, positive ions, and neutrals. They are related by $\eta_+ = \eta_e + \eta_-$ and $\eta_n = \eta_{n0} - \eta_+ - \eta_-$ where η_{n0} is the initial neutral number density. ν_{photo} is the rate that electrons are photodetached from negative ions. For a 3.9 μm laser driver this occurs through 2-photon multiphoton ionization, discussed previously in Section 1.3. At 0.1 TW/cm^2, ν_{photo} is greater than 10^{18}/s, resulting in full ionization of the O_2^- population during the rising edge of the drive pulse. ν_{coll} is the electron-neutral collisional ionization rate [14]. ν_a is the rate at which electrons attach to neutral oxygen to form the negative O_2^- ion [47]. β_{e+} is the rate at which electrons recombine with positive ions [48]. β_n is the rate that electrons detach from negative ions through collisions with neutrals [48]. $\beta_{\pm}$ is the rate at which a negative and a positive mutually neutralize each other [48]. The laser heating term, $U_p\nu_e$, is described earlier in Section 1.2. $\dot{\varepsilon}_{loss}$ is a total energy loss term for electrons

including vibrational and rotational excitation of molecules and other loss mechanisms [49]. In general, these terms are all temperature dependent.

In the presence of a radioactive source, an additional free-electron generation term, ν_{rad} can be added accounting for the energy deposition of the high-energy radioparticles emitted by the source. For Po-210, the decay product is a 5.4 MeV α-particle. In a foil source, the Po-210 is embedded behind approximately 1.5 μm gold foil and 0.3 μm nickel foil [50]. Energy loss through these thin but dense layers reduces the peak energy of α-particles leaving the surface to about 4.7 MeV.

We track the energy deposition of an α-particle as it travels through air using the continuous slowing down model and linear stopping powers from NIST ASTAR [35]. For particle energies greater than 100keV, almost all of the energy loss is from electronic interactions. We use the approximate value 35eV of energy deposition per ionization event, accounting for both energy losses to ionization and nonionizing electronic excitations [51].

Under no laser driving, we can find the steady state solutions to the simplified set of equations, removing all of the laser-driven terms. We can also neglect the electron recombination term that is very small for weak ionization.

$$\frac{\partial \eta_e}{\partial t} = \nu_{rad} - \nu_a \eta_e + \beta_n \eta_n \eta_-$$

$$\frac{\partial \eta_-}{\partial t} = \nu_a \eta_e - \beta_\pm \eta_+ \eta_- - \beta_n \eta_n \eta_-$$

which yields the steady state solutions $\overline{\eta_e} = \frac{\nu_{rad}}{\nu_a} + \frac{\beta_n \eta_n}{\nu_a}\sqrt{\frac{\nu_{rad}}{\beta_\pm}}$ and $\overline{\eta_-} = \sqrt{\frac{\nu_{rad}}{\beta_\pm}}$.

Figure 2.9(a) shows the energy loss of a single 4.7 MeV α-particle as it travels through dry air (red curve), and the resultant energy deposition in air from a 5mCi Po-210 source (blue curve), taking into account $1/r^2$ scaling. The large stopping power for α-particles even in a low-density material like air means that all the energy is deposited within 3cm. Figure 2.9(b) shows the steady state electron and O_2^- densities that result from irradiation from that source. The O_2^- densities are typically many orders of magnitude higher than the free electron densities so that to the total charge is almost entirely contained in the O_2^- population. From this, we can see that the total enhanced charge density from a radiation source scales like the square root of the irradiation.

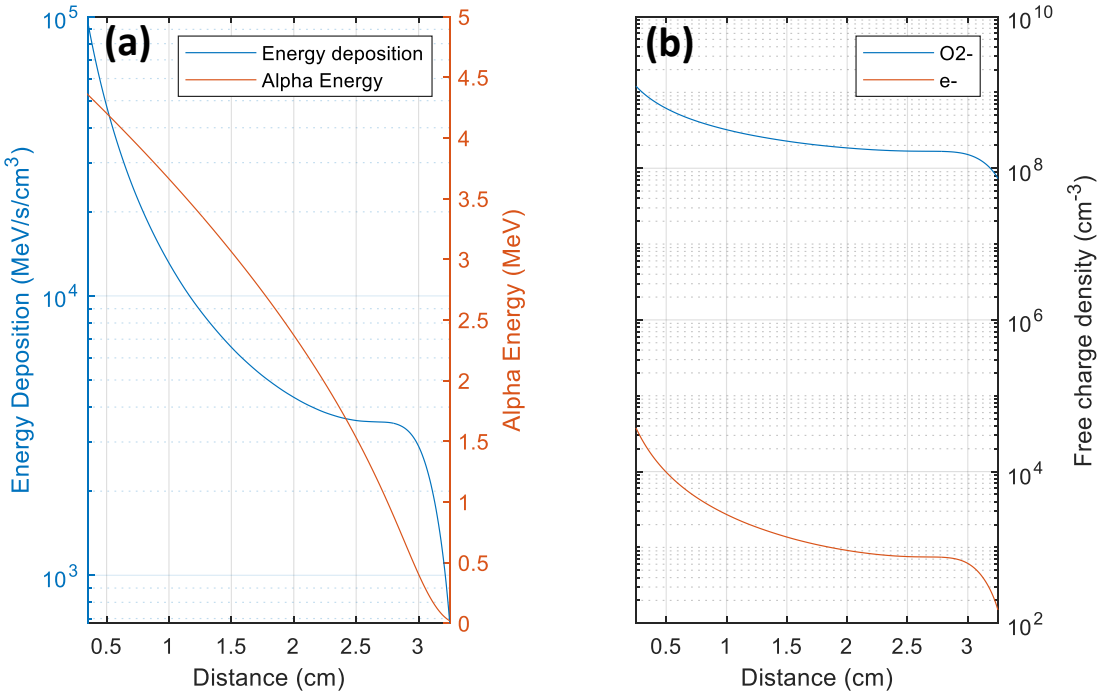

Figure 2.9 Free charge generation from radioactive sources. (a) shows the energy (red) of a single 4.7 MeV α-particle as it travels through air and the rate of energy deposition (blue) from a 5mCi source in air. (b) shows the steady-state free electron and O_2^- densities as a function of distance from the Po-210 source.

2.4.2 Time Advance Calculations

Calculating the time advance from laser parameters and seed density requires correlating the focal geometry with the seed density. For a Gaussian beam of peak intensity I focused to a spot radius w_0, the total volume in which the intensity is greater than the breakdown threshold I_{th} is given by [27]

$$V_{th} = \frac{\pi^2}{3}\frac{w_0^4}{\lambda}\left\{\frac{2}{3}\left(5 + \frac{I}{I_{th}}\right)\sqrt{\frac{I}{I_{th}} - 1} - 4\tan^{-1}\left(\frac{I}{I_{th}} - 1\right)\right\}$$

For low seed densities, the plasmas from each seed electron grow independently. The breakdown rate for each plasma is found by solving the rate equations from Section 1.5 where the laser intensity is determined by the position of the seed electron with respect to the drive laser's focus. The observed breakdown time depends on the random placement of the seed electrons with the focal volume. Breakdowns occurring near the laser focus see a higher peak intensity and earlier breakdown times.

The average number of breakdowns in the focal volume is $N = \eta_e V_{th}$. For $N \gg 1$, there will almost always be a seed electron very close to the laser focus, so the breakdown timing will be nearly deterministic. Conversely, for $N \ll 1$, there will either be no breakdown, or breakdowns where a single electron is randomly found anywhere in the focal volume. In this case, the breakdown timing will only be weakly correlated to the seed density. For $N \approx 1$, there is a high sensitivity between breakdown time advance and seed density. The breakdown time statistics can be found using a Poisson distribution of seed electrons.

We can calculate the time advance for a given distribution of seed electrons by breaking the focal volume into discretely binned regions of constant intensity. The time advance is given by the probability of finding an electron at intensity I without having any electrons in regions of higher

intensity. For a seed density n_e in a volume V, the mean number of electrons in a given volume is $N = \eta_e V$. The probability of finding X electrons within that volume is given by $P(X) = {N^X e^{-N}}/{X!}$. The probability of finding no electrons in a given volume is then $P(0) = {N^0 e^{-N}}/{0!} = e^{-N}$. Similarly, the probability of finding at least one electron is then just $P(\geq 1) = 1 - P(0) = 1 - e^{-N}$. So for a given intensity I occupying volume V, with volume V' being the volume with intensity $I' > I$, the probability that at least one electron is in V and no electrons are in V' is given by $P(I) = e^{-N'}(1 - e^{-N})$.

For a λ=3.9 μm, τ=50 ps laser pulse, the expected breakdown time advance statistics are shown in Figure 2.10. We first consider the evolution of a single breakdown. Figure 2.10(a) shows the breakdown time advance, defined when the plasma density reaches 10^{18} cm^{-3}. Below the threshold intensity, 1.6 TW/cm^2, the plasma does not reach 10^{18} /cm^3 so there is no time advance. For *f*/20 and *f*/33 focusing with a peak intensity of 2.25 TW/cm^2, Figure 2.10(b) shows the calculated mean and standard deviation of the time advance for seed densities between 10^3 and 10^7 /cm^3. There will be an average of one electron in the focal volume for *f*/20 focusing when the seed density is 1.7×10^5/cm^3, and for *f*/33 when the seed density is 2.2×10^4 /cm^3. The larger focal volumes generated by slower *f*/# geometries shifts the sensitivity to lower seed densities. Once the seed density is sufficiently high, there is a very high probability that one will be located near the beam waist. This leads to a saturation in the time advance and reduction in the variability. From

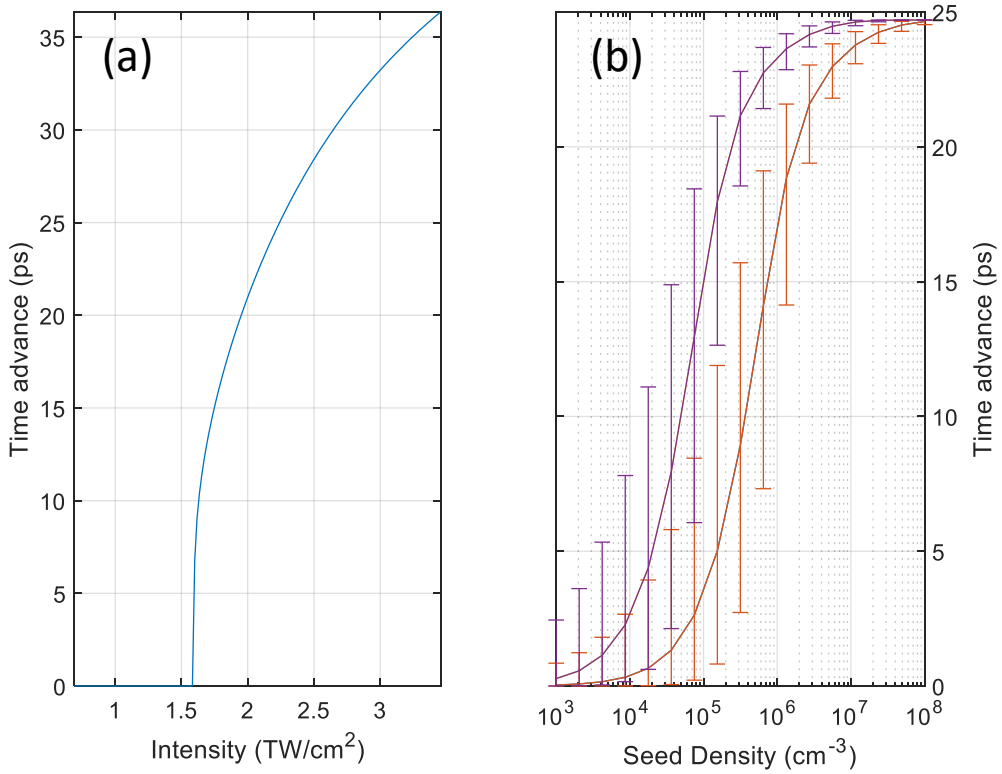

Figure 2.10 Calculations of breakdown time advance for a 3.9 μm, 50ps laser pulse. **(a)** shows the time advance for single breakdown as a function of peak laser intensity. **(b)** shows the mean and standard deviation of time advances as a function of seed density for *f*/20 and *f*/33 focusing geometries.

Figure 2.10(a), we see that the fastest breakdowns for a peak intensity of 2.25 TW/cm^2 will have time advances of around 25 ps.

2.4.3 Scattering from Avalanche Plasmas

The scattering diagnostics described in the above experiments rely on the size and density of the plasmas to be sufficiently high to scatter enough of the laser pulse to be detectable. We can consider the case of a plasma created by a single seed electron using our backscattered mid infrared spectrometer diagnostic. Described earlier in sections 1.4 and 1.5, we can take the radius of the

plasma to be limited by diffusion to about 4 μm for a 3.9 μm laser. The plasma refractive index is a function of the ratio between the plasma density η_e and the critical plasma density η_{crit}

$$n_{plasma} = \sqrt{1 - \eta_e \,/\, \eta_{crit}} \approx 1 - \eta_e \,/\, 2\eta_{crit}.$$

Treating each plasma sphere as a simple reflecting boundary we have a reflection coefficient $R = \left|\frac{1-n_{plasma}}{1+n_{plasma}}\right|^2 \approx \frac{\eta_e^2}{16\eta_{crit}^2}$. The breakdowns are detectable with time advance τ_{adv}. For a beam waist w_0 and a total pulse length τ_{pulse}, the fractional backscattered energy is given by $R\frac{\tau_{adv}}{\tau_{pulse}}\frac{r_{plasma}^2}{w_0^2}$. We can further assume this energy will spread uniformly over 2π solid angle. The efficiency of the light collection is given by $\sigma = \frac{\pi d^2}{2\pi f^2} = \frac{1}{2}(f/\#)^{-2}$.

We can consider the case for a 3.9 μm beam focused at *f*/20 to intensity 2.25 TW/cm^2. From Section 2.4.2 we see that the time advance will be about 25 ps. The collected energy at the spectrometer will be

$$E_{spec} = I\frac{\eta_e^2}{32\eta_{crit}^2}\frac{\tau_{adv} r_{plasma}^2}{(f/\#)^2}$$

This energy will be dispersed through the spectrometer onto the sensor. We assume the efficiency of the spectrometer is perfect. The pixel dispersion of the sensor is approximately 0.2 ps/pixel, its quantum efficiency in the spectral range of the laser is about 90%, and each count requires approximately 400 electrons. This gives a count per pixel of

$$\#_{pixel} = E_{spec}\frac{\tau_{pixel}}{\tau_{adv}} \times \frac{QE}{400} \times \frac{\lambda}{hc}$$

The noise floor on the detector is about 2 counts, so we can find the minimum plasma density needed to have a unity signal to noise threshold $\#_{pixel} = 2$.

$$\eta_{thresh} = 160 \frac{\eta_{crit} \times (f/\#)}{r_{plasma}} \times \sqrt{\frac{hc/\lambda}{I \times \tau_{pixel} \times QE}}$$

For the conditions described above this gives a threshold plasma density for a detectable signal of about $8 \times 10^{17}/\text{cm}^3$, extremely close to our best-guess approximation of 10^{18} /cm^3.

Chapter 3: Measurements of high field ionization using avalanche breakdowns

3.1 Introduction

Introduced in Section 1.3, the theory of multiphoton and tunnel ionization described by Keldysh [13] was crucial for further basic research into high intensity laser-matter interactions [17,47–50]. In this unified theory of ionization, lasers can free electrons from atoms and molecules with ionization potentials greater than the photon energy. At moderate intensities, the behavior is described as multiphoton ionization (MPI), where multiple photons are simultaneously absorbed, with their total energy greater than ionization potential. In this regime, the ionization rate: $\nu_{MPI} \propto I^N$, where N is the integer number of photons needed to surpass the ionization potential. At higher intensities, the mechanism transitions towards tunneling ionization, where the laser field suppresses the atomic Coulomb potential sufficiently for an electron to tunnel though the reduced effective field. In this case, the ionization rate has a reduced dependence on the field strength: $\nu_{tunnel} \propto I^{N'}$, where $N' < N$. The transition between MPI and tunneling is characterized by the dimensionless Keldysh parameter: $\gamma_K = \sqrt{\varepsilon_{ion}/2U_P}$, where ε_{ion} is the ionization potential of the atom or molecule and U_P is the ponderomotive energy of the laser field. The multiphoton regime occurs when $\gamma_K \gg 1$, and the tunneling regime is dominant when $\gamma_K < 1$.

While the earliest experiments in laser ionization [3,4] demonstrated that nonlinear ionization is an important process, it wasn't until short pulse laser technology allowed significantly higher laser intensities to measure ionization rates across the transition into the tunneling and over-the-barrier regimes [52–55]. Early ionization measurements used

microchannel plates to collect ions, requiring experiments to take place at low gas densities (typically around 10^8 to 10^{12} cm^{-3}) to avoid space charge effects and interactions with remaining neutrals. However, many applications of high intensity laser-matter interactions, such as high harmonic generation [56] or filamentation [57,58] occur at significantly higher densities, where density dependent effects may play a role in ionization.

Electron-induced dephasing (EID) is a recently proposed mechanism in which the interactions between nearby electrons can lead to enhanced ionization at lower laser intensities at high gas densities [1,59–61]. Standard theories of nonlinear ionization can be thought of as a field-induced dephasing of the bound state-continuum coherence, reducing the adiabatic following of electrons in the strong, detuned laser field. EID proposes that electrons in the continuum state can interact with the long range, poorly screened Coulomb fields of other nearby electrons, providing an additional source of dephasing and increased ionization yields.

The ionization predicted by EID from [1] is shown in Figure 4.1 for λ=1 and 10 μm, 100 fs laser pulses in Hydrogen at 1 atm. The ionization yield from EID scales sublinearly with neutral density and quadratically with intensity, with minimal dependence on laser wavelength or gas species. This strongly diverges from standard nonlinear ionization models that scale linearly with density and have a strong intensity dependence based on the photon energy and gas species. The contribution from EID is only apparent at low intensities, where the steeper MPI curves quickly vanish, while the I^2 enhancement from EID begins to dominate. At higher intensities, the EID contribution is negligible compared to the large yields from traditional single-atom models.

Despite the low ionization yield predicted by EID, its potential effects can be significant, especially at longer wavelengths where low plasma densities can still lead to a significant effect on the refractive index. A recent experiment on filamentation with a λ=10 μm CO_2 laser with

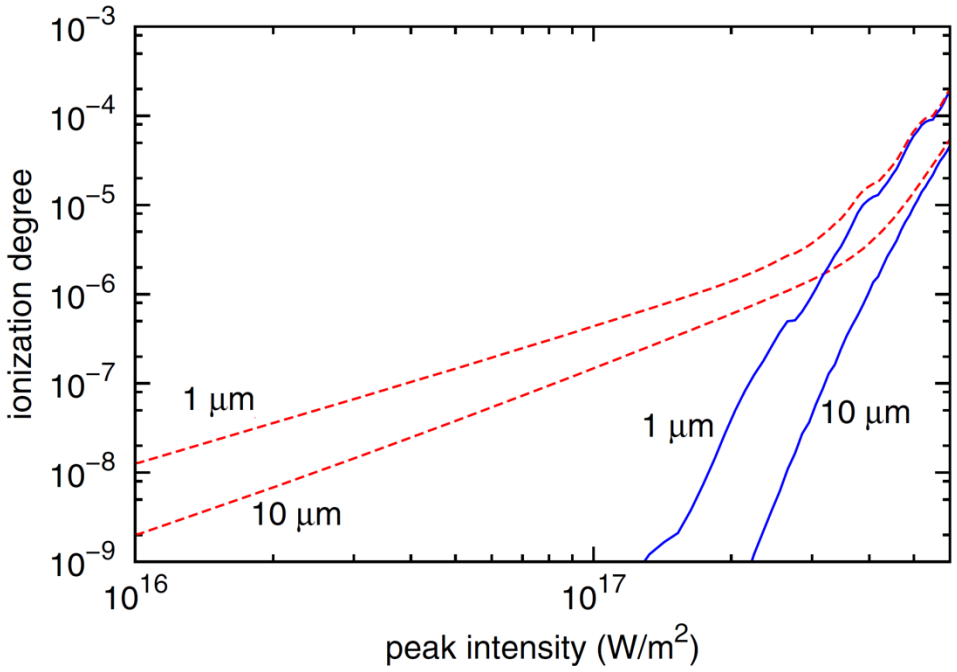

Figure 3.1 Predictions of EID many-body ionization contributions (red dashed lines) and single-atom ionization models (blue lines) from [1]. Calculations are performed for a 100 fs FWHM cosine squared pulse with wavelength λ=1 or 10 µm in atmospheric pressure hydrogen.

peak intensities around 1 TW/cm^2 observed channeling over approximately 20 Rayleigh ranges in air [62]. At this low an intensity, single-atom models do not predict any appreciable ionization needed to counteract Kerr self-focusing, so EID was a proposed arrest mechanism leading to a long, low intensity filament. Additionally, the radiation detection experiments described in Chapter 2 rely on the mid-infrared driver not appreciably multiphoton ionizing neutral air molecules, contributions from EID could play a significant role in these measurements. Shown in Figure 3.1, at 1 TW/cm^2, EID predicts an ionization yield of 10^{-8}-10^{-9} for λ=1 and 10 µm, 100 fs laser pulses. For a 50 ps pulse, the expected ionization would be about 500 times greater, generating plasma densities of 10^{13} to 10^{14} / cm^3 and completely washing out any smaller signals from radiation enhancement.

Measurements of ionization rates with λ=800 nm lasers in atmospheric pressure gasses using microwave scattering [63] and single-shot supercontinuum spectral interferometry [64] have shown good agreement with standard ionization models. These diagnostic techniques are limited in their sensitivity, and have only probed ionization yields greater than ~10^{-5}, above the threshold where EID has a significant impact.

Following the avalanche based measurements used for radiation detection, we can extend the technique to measure laser ionization yields [43]. Here, we use our mid-infrared picosecond laser as a probe pulse to measure the absolute ionization yields from femtosecond near- and mid-infrared laser pulses in atmospheric pressure range air, nitrogen, and argon. This method is extremely sensitive and by exploiting the focal geometry of the two lasers, can measure ionization yields across an unprecedented 14 orders of magnitude: from 10^{-16} to 10^{-2}.

3.2 Experimental Outline and Methods

Our measurements used two beams. First is the chirped 50 ps λ=3.9 μm probe pulse which is used to drive avalanche. Described earlier in Chapters 1 and 2, mid-infrared short pulse laser driven avalanche ionization is an effective tool for amplifying and measuring extremely low density plasmas. This pulse is focused to a spot size of w_0=70 μm with peak intensity of 1-1.5 TW/cm^2. The second pulse is either a near-infrared (λ=1024 nm, 274 fs) or mid-infrared (λ=3.9 μm, 85 fs) drive pulse which directly ionized neutrals creating a seed population for the avalanche breakdowns. The beam energies of these pulses are controlled with a waveplate and polarizer and focused to intensities in the range 1-100 TW/cm^2. All the beams are generated in the generated from the same OPCPA system and are optically synchronized [32–34].

Figure 3.2 shows the experimental outline with three focal geometries and two diagnostics used. For low seed densities, direct imaging allows each breakdown to be counted. As described in Section 1.4, each breakdown site will grow to approximately 10 µm in diameter, so for low ionization yields $Y < 10^{-11}$, the breakdowns remain isolated and were measured with a 16-bit low-noise CMOS camera (Thorlabs Quantalux) shown in Figure 3.2(a). These experiments were performed in a sealed gas cell filled with either air, nitrogen, or argon with an inline 0.01 micron particulate filter to reduce the probability of dust entering the vessel.

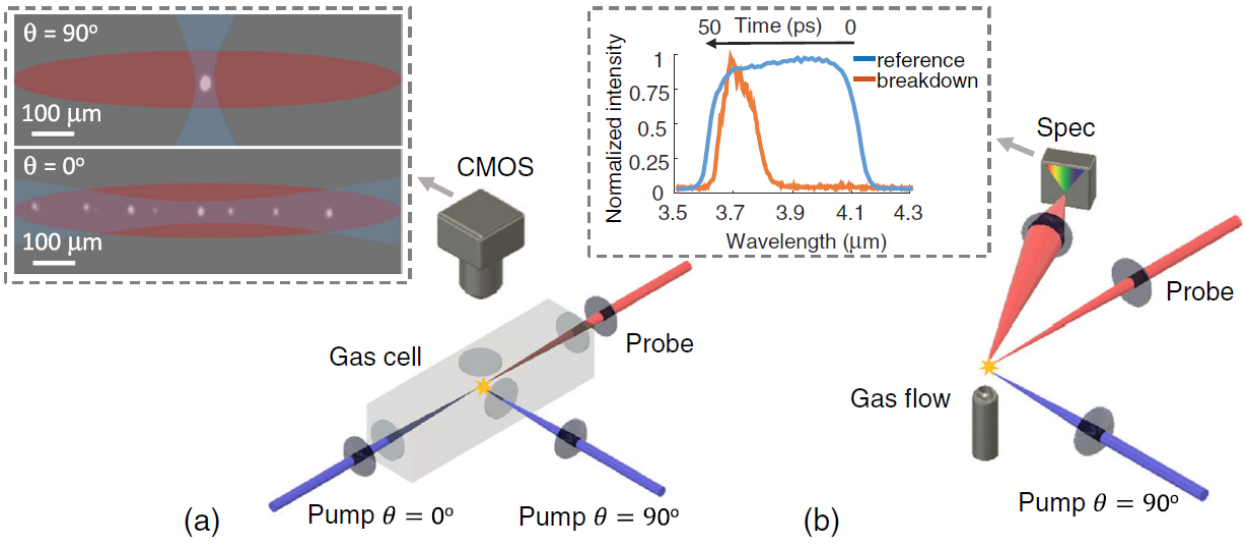

Figure 3.2 (a) A direct breakdown imaging system was used for low pump intensities (< 10 TW/cm$^{2)}$. A chirped λ=3.9 µm 50 ps probe pulse is focused into a gas cell to drive avalanche ionization from free electrons. A pump pulse (λ=1024 nm 274fs or λ=3.9 µm 84 fs) either counter-propagating or transverse to the probe beam generated free electrons through nonlinear ionization. For each geometry, the inset shows the overlap between the two beams, defining the volume probed by the avalanche breakdowns. The visible plasma emission is measured with a CMOS camera. **(b)** Backscattered probe spectrum is used to measure higher pump intensities (<100 TW/cm^2). The spectrum of the backscattered probe (example in inset) is correlated to the seed electron density generated through nonlinear ionization of the transverse probe.

The sensitivity of this set up is determined by the probed volume defined by the overlap of the two beams. Two geometries were used: a counter-propagating θ=0° pump and a transverse θ=90° pump. The beam overlaps of the two geometries are shown in the inset to Figure 3.2(a). For lower intensities, the counter-propagating geometry maximizes the beam overlap and increases the sensitivity to lower pump intensities and ionization yields. To avoid refocusing the λ=3.9 μm beam back into the laser we only used the λ=1024 nm beam in this geometry, focused to a spot size of w_0=30 μm. When the number of breakdowns reaches ~10, propagation effects from upstream plasmas become significant, discussed in Section 3.3.4. In this case, we transition to the transverse pump geometry that reduces the beam overlap by a factor of 100. The λ=3.9 μm pump was focused to w_0=30 μm, and the λ=1024 nm pump was focused to w_0=26 μm. Although this geometry restricts the number of reliably counted breakdowns to one, by taking a large number of shots we can infer a mean number of breakdowns up to a Poisson mean of four based on the number of zero counts: $P(0) = 1 - e^{-\mu}$. To find the peak yield Y_0 corresponding to the pump laser peak intensity I_0 from the total breakdown number N we use

$$N = \int_V Y_0 \left[\frac{I(r,z)}{I_0}\right]^m dV$$

where $I(r,z)$ is the spatially varying pump intensity, m is the MPI scaling exponent, and V is the overlap volume of the two beams.

At higher ionization yields, direct counting is no longer feasible to the high density of seed electrons leading to overlapping plasma growth. In this regime, we can treat the breakdown as a continuous plasma rather a collection of discrete sites. We therefore have a deterministic breakdown duration, determined by the starting seed density and the growth rate:

$$\tau = \ln\left(\frac{\eta_f}{\eta_i}\right)/\nu_{ion}$$

where η_f is the density at which the plasma is detectable, η_i is the seed density generated by the pump's ionization, and ν_{ion} is the collisional ionization rate. Following the backscatter spectrum measurements in Section 2.3, we can record a time advance given by the probe laser's pulse length, 50 ps, subtracted by the breakdown time duration τ. Figure 3.2(b) shows the experimental layout for these measurements as well a reference and sample breakdown spectrum. The wavelength-to-time conversation is measured though a cross-correlation between the chirped λ=1450 nm signal beam in the OPCPA and the femtosecond λ=1024 nm beam, with a known conversion into the idler λ=3.9 μm given by $\lambda_{idler} = 1/\left(\frac{1}{1064\text{ nm}} - \frac{1}{\lambda_{signal}}\right)$.

3.3 Breakdown Counting Results

Figure 3.3 shows the ionization yields measured at low pump intensities (0.6 to 10 TW) using direct imaging and counting of breakdowns. In Figure 3.3(a), the ionization yield in atmospheric pressure for the λ=1024 nm pump is shown, for both counter-propagating and transverse geometries. The left-hand vertical axis shows the average number of breakdowns counted, with different scales for the two beam crossing geometries. The right hand vertical axis shows the calculated yield. The blue squares showing the counter-propagating geometry and the red squares showing the transverse geometry are shifted horizontally with respect to each other, due to approximately 10% uncertainty in the peak laser intensity shown by the green horizontal bars. The yellow triangles show the counts for the transverse geometry using a calculated Poisson mean from the number of zero breakdown counts. While this leads to mean counts greater than the number of observed sites, it corrects for the inability to resolve multiple breakdowns from our imaging system. At this wavelength and range of intensities, the Keldysh parameter $\gamma_K > 3$ for ionization in air, so we can expect a reasonable fit to an MPI model where $Y \propto I^m$. The black dashed line

shows fits for the counter-propagating and uncorrected transverse crossing data for m=5.5, fitting both curves well for peak intensities below 4 TW/cm^2. At the higher intensities using the Poisson-corrected transverse data, a fit with m=9.7 shows good agreement, corresponding to average ionization potentials of 6.7 eV and 11.7 eV, respectively.

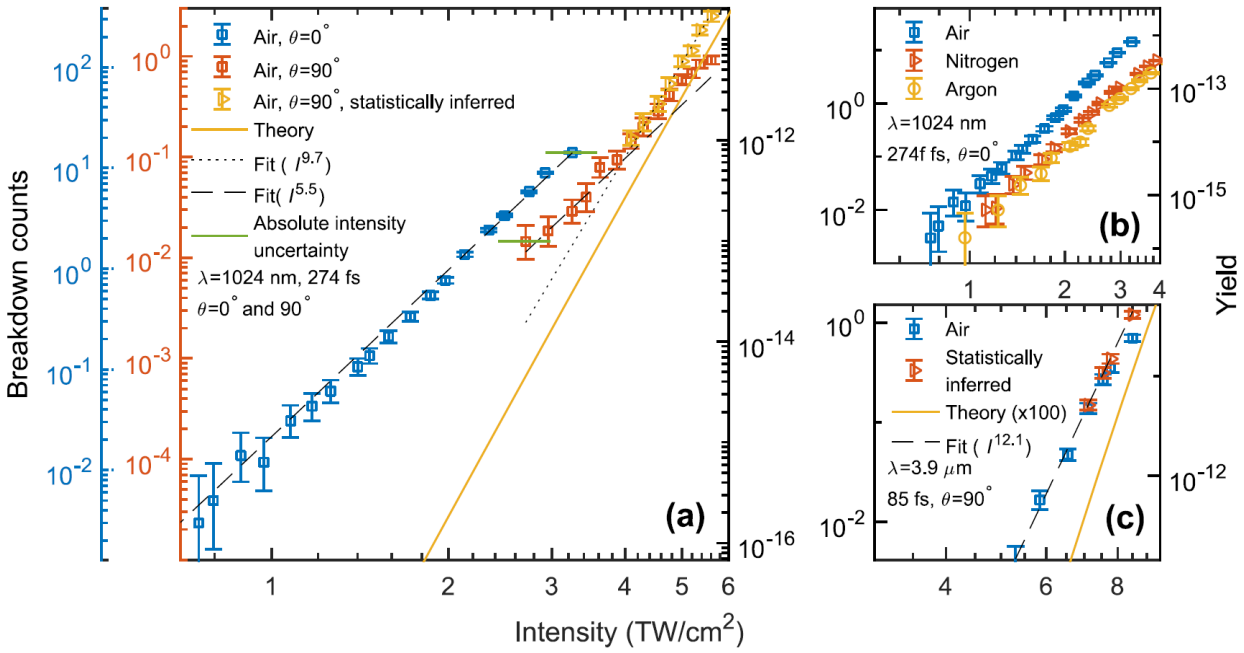

Figure 3.3 Ionization yield measurements using direct breakdown imaging. **(a)** Measurements for the λ=1024 nm pump. The left vertical axis shows the total breakdown counts for the counter-propagating (blue) and transverse (red) geometries. The right vertical axis shows the correlated total ionization yield. The yellow triangles show the breakdown counts inferred from Poisson statistics. The data is fit to two empirical MPI curves, shown in the dashed and dotted black lines. The yellow curve shows the theoretical ionization rate for air. **(b)** Comparison of ionization yields for the λ=1024 nm pump in air, nitrogen, and argon gasses. **(c)** Ionization yields for the λ=3.9 μm pump. The blue squares show the total breakdown counts, while the red triangles again show the statistical corrected values. The dashed line shows an empirical MPI fit, and the yellow line shows the theoretical ionization yield scaled up by a factor of 100.

Figure 3.3(c) shows the measured yields from the λ=3.9 μm pump in air, again including the uncorrected and Poisson-corrected values. A fit to an exponential model is shown with the dashed line for m=12.1, corresponding to a 3.9 eV ionization potential. The Keldysh parameter for these intensities range are $\gamma_K \sim 1$ so although a pure MPI fit may not accurately resolve the ionization potential of the gas, it still is a benchmark for the underlying ionization mechanism. The yellow curve in Figures 3.3(a,c) show the theoretical ionization curve for single-molecule interactions [13,19] in air comprised of 80% N_2 and 20% O_2, using empirical values for the effective potentials [55]. The theoretical model matches with a factor of 2 to our measurement at high intensities for the λ=1024 nm pump, but our measurements are significantly higher than predicted at lower intensities and with the mid-infrared pump. The abrupt change in the scaling from the expected 12.1eV multiphoton ionization for oxygen to the lower 6.7eV or 3.9eV ionization potentials is evidence of either a ubiquitous contaminant or some other mechanism such as EID.

To further identify the source of this anomalously high low-intensity ionization, we compared the yields for air, nitrogen, and argon using the λ=1024 nm pump in the counter-propagating geometry. Shown in Figure 3.3(b), all three curves show nearly identical $I^{5.5}$ scaling with intensity, despite the different ionization potentials of the gasses. The nitrogen and argon used were high purity bottled gasses (<2 ppm water, <0.1 ppm hydrocarbon) while the air source was from a facility compressed air line filtered for oil, water, and particulates. Scaling the gas from 0.5 to 3 atm does not change the scaling at low intensities. The intensity scaling and lack of pressure dependence contradicts predictions from multi-body effects and further suggests the ionization is due to some contaminant.

We compared the ionization yields for two sources of air: the particulate filter compressed air line and a bottled ultrapure air (<2 ppm water, <0.1 ppm hydrocarbon) further filtered with an activated charcoal filter (Supelcarb) capable of absorbing primary hydrocarbons down to the ppb level. For the transverse λ=3.9 μm pump the ionization yields of the two air sources are shown in Figure 3.4. We see that the shape of both curves is identical, but the filtered bottled air source reduces the ionization yield by a factor of 4. Since the only difference between the two sources is the concentration of trace impurities, we attribute the anomalously high low-intensity ionization yield to the ubiquitous presence of an unidentified, low ionization potential impurity.

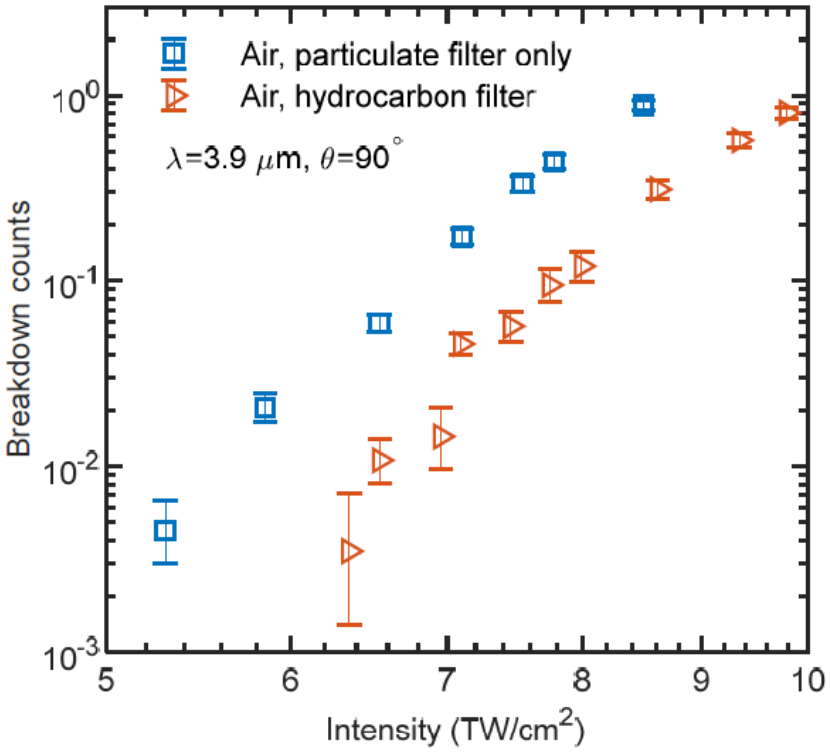

Figure 3.4 Ionization rates for two sources of air. The blue squares show measurements for laboratory compressed air passed only through drying filters and a particulate filter. The red triangles show measurements using ultra-high purity bottled air passed through a high efficiency hydrocarbon filter. The reduction in breakdown counts observed in higher purity air is evidence of a low ionization potential ubiquitous contaminant.

3.4 Self-Seeded Ionization Measurements

For the mid-infrared pump, only the transverse geometry is feasible to avoid sending the pulse back through the laser, limiting the lowest measurable intensity to 5 TW/cm^2. We can test lower intensities using only the avalanche-driving probe laser, where the seed electrons are either present in background air or generated by the leading edge of the pulse. Figure 4.5 shows results for peak probe intensities between 1.5 and 1.8 TW/cm^2. Due to a single pulse being used to both create the seeds and amplify them to detectable levels, we need to make several corrections to directly compare the results from different intensities. First, high intensities probe larger volumes, as discussed in Section 2.3.4. Second, higher intensities drive the avalanches faster, which means there is more time for seeds to be generated through multiphoton or tunnel ionization while still having time for the avalanche to build to detectable levels. Discussed in Section 1.2, the ionization rate can be treated as approximately linear with intensity, so we can scale the effective times over which generated seed electrons can be detected linearly. While a full calculation to convert measured counts to absolute ionization yields would require a more detailed treatment, this simplistic scaling is sufficient to determine how ionization scales with intensity. The corrected breakdown counts scale exponentially with $m \approx 19$, corresponding to approximately 6.1 eV ionization energy, in closer agreement with the low-intensity ionization yield with the near-infrared pump.

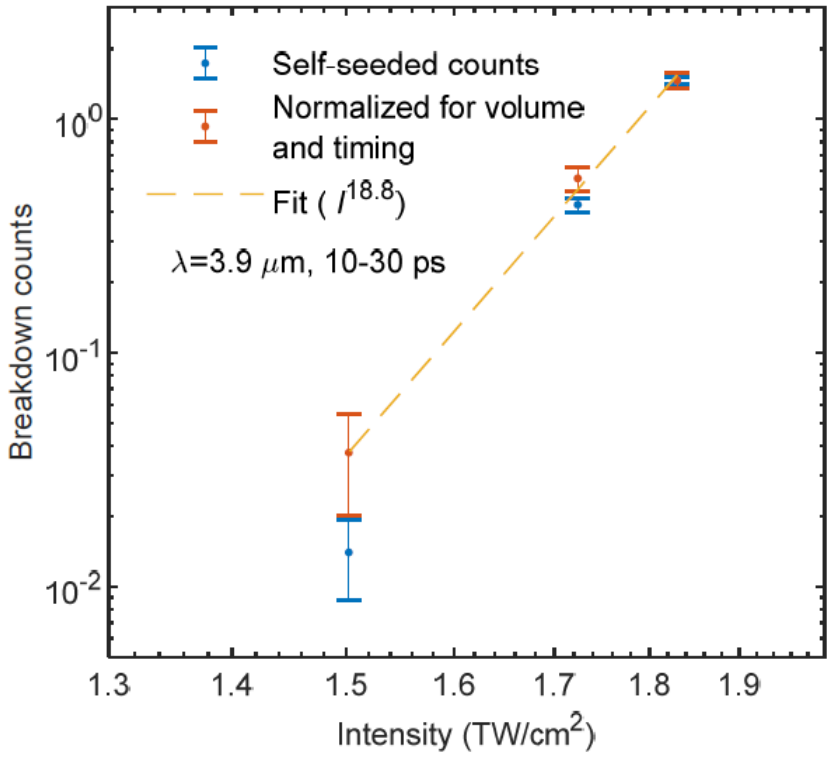

Figure 3.5 Measurements of self-seeded avalanche breakdowns using only the probe pulse. Here, the leading edge of the probe pulse can weakly ionize the air, liberating electrons which are amplified through avalanche ionization later in the pulse. The blue measurements show the observed breakdown counts, while the red measurements show the data corrected for volume and timing scaling. The yellow dashed line shows an empirical fit to an MPI model.

3.5 Ionization of a 6 eV Contaminant

We can compare the results to theoretical ionization yields from a 6eV contaminant [19], shown in Figure 3.6. Since the identity of the contaminant is unknown, two cases are considered. The first is a simple atom, with an effective Coulomb potential $Z_{eff} = 1$. The second is molecule with a $Z_{eff} = 0.5$, a reasonable lower bound of the effective potential for a larger molecule [55]. Data from both seeded and unseeded breakdowns are included and rescaled to overlap onto the calculated curves. The self-seeded data is scaled to account for intensity dependent pulse length and probed volume then normalized for comparison with the 85 fs transverse geometry.

The scaled data for both near- and mid-infrared ionization yields closely match the theoretical curves for a 6 eV contaminant with $Z_{eff} = 0.5$ for all gasses tested. Based on the theoretical ionization fraction and the measured ionization yields, the contaminant is present at concentrations of approximately 10^{-11} to 10^{-9}. Earlier work measuring residual gas in a partially evacuated vacuum chamber found the presence of low ionization potential contaminants on all laboratory gasses and credited these as the seed electrons for early avalanche breakdown experiments [65]. The technique was not able to accurately resolve the total concentration of these molecules however. Another ionization study in air using a λ=248 nm ($E_{photon} = 5$ eV) laser saw a linear scaling of ionization yield with intensity between 10^6 and 10^9 TW/cm^2, before the expected 2-3 photon ionization of air molecules at higher intensities [66]. The electron density measured through plasma conduction in the linear ionization regime reached approximately 10^{10} /cm^3, corresponding to a concentration of around 10^{-9} assuming full ionization of the contaminant and negligible ionization of further air molecules.

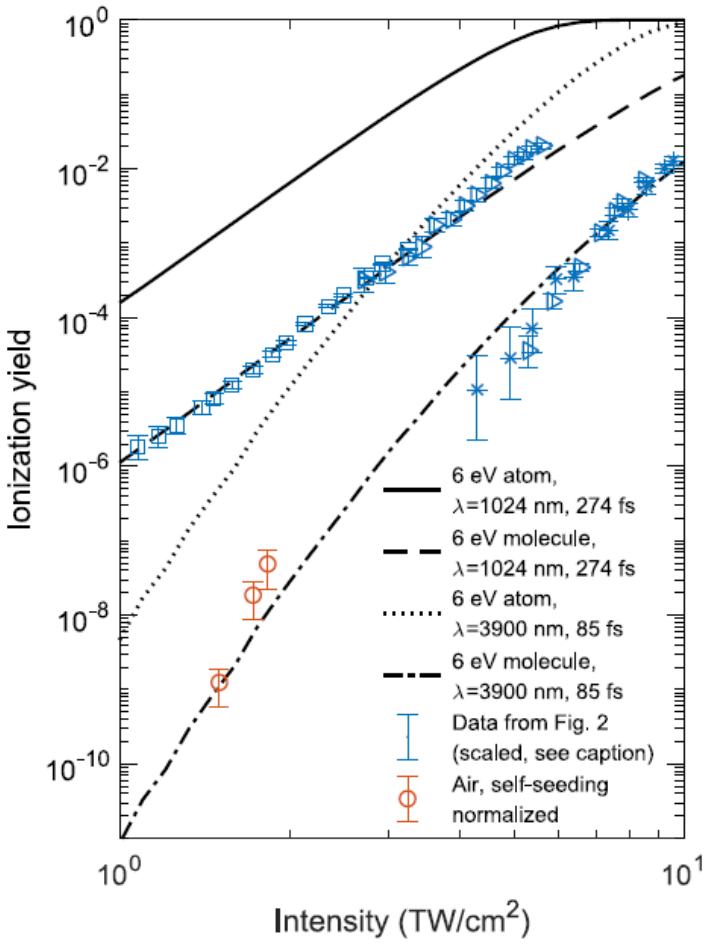

Figure 3.6 Comparison between out observed measurements of a 6eV contaminant and theoretical models. The blue data shows results from Figure 4.3, shifted to overlap with theoretical curves. The red data shows results from Figure 4.5 normalized and scaled to the other femtosecond data shown on the plot. The four theoretical curve show ionization of a 6 eV particle with our near- and mid-infrared pump pulses for both an atomic model (Z_{eff}=1) and a molecular model (Z_{eff}=0.5).

3.6 Breakdown Time Advance Measurements

Ionization measurements at higher intensities were measured using the breakdown time advance as measured by the backscattered spectrum of the probe pulse. In this regime we can resolve the transition from MPI into the tunnel ionization regime for λ=1024 nm in air and nitrogen for intensities up to 100 TW/cm^2.

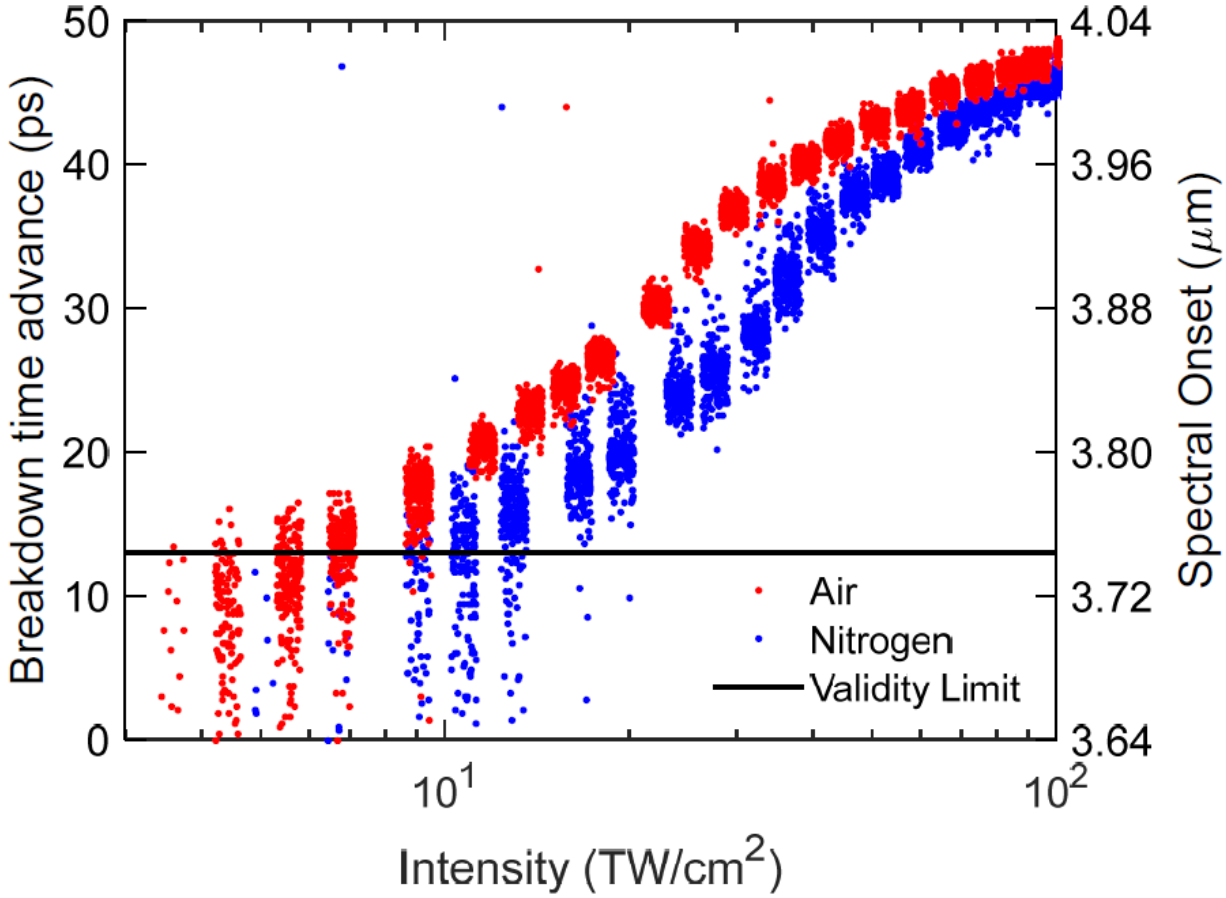

Figure 3.7 Single shot measurements of breakdown time advance in air and nitrogen. Each point corresponds to the breakdown timing of a single shot, showing both the spectral onset of the backscattered signal (left) and the corresponding breakdown time advance (right). The horizontal line corresponds to the regime where breakdown time advance is well-correlated to the pump's ionization yield.

The results of single shot breakdown timing for intensities are shown in Figure 3.7 for ionization in air and nitrogen. Following the calculations discussed earlier in Section 2.4.2, the breakdown time advance is determined by the rate at which the fastest growing avalanche breakdowns reaches sufficient density to efficiently scatter the λ=3.9 μm probe laser. For relatively low seed densities, such that only a few electrons are located in the focal volume, the

time advance is highly variable. The measurements for different shots are determined by the location of the electron closest to the beam focus where the intensity highest, leading to poor sensitivity to the actual seed density. At greater seed densities, although the exact placement of those electrons is random, there is better defined distribution throughout the focal volume. In this regime, while still variable, the seed density closely correlates to the average peak intensity experienced by a seed electron, leading to a more deterministic breakdown time advance. Once the density is high enough that the separation between seed electrons is smaller than the diffusion length of the avalanche plasma ($r_d \sim 4$ μm), the plasma can be treated continuously, with higher seed densities effectively decreasing the number of doubling generations needed to reach a detectable density. We limit our analysis to the region where seed densities are well-correlated to time advance. This limit is set at ionization yields greater than 7×10^{-11}, corresponding to 10 times the yield corresponding to one shot per breakdown from Figure 3.3.

We calibrate the measured time advance to ionization yield through comparisons with the direct counting measurements at 6 TW/cm^3 and theoretical values at 100 TW/cm^2 with direct interpolation between these extremes using a constant avalanche growth ν_i. Because measurements of the ionization yield in O2 and N2 with a 42 fs, λ=800 nm laser pulse in a thin gas jet [67] showed excellent agreement with theoretical rates [19], we use this model to determine the yield at our highest intensity. Interpolating between these two limits gives an electron density growth rate of $\nu_i = 0.55$ /ps, which we use to calculate the conversion between time advance and ionization yield at intermediate intensities.

Figure 3.8 shows the ionization yields from the time advance measurements for air and nitrogen. Overlaid in yellow are the theoretical single-body ionization curves. The measured yields agree within an order of magnitude to the theoretical predictions for all intensities, with values

slightly overestimating the predicted yields. We attribute some of the overestimation to our constant avalanche growth rate. The heating is proportional to $I\lambda^2$, so the redder, earlier portions of the beam will cause greater heating. Further, the chirped pulse is not perfectly flat top, but has somewhat higher intensity on the red side (see inset to Figure 3.2). Both of these effects will lead to a more rapid early growth rate, slightly suppressing the measured yield and bringing it closer to the theoretical values.

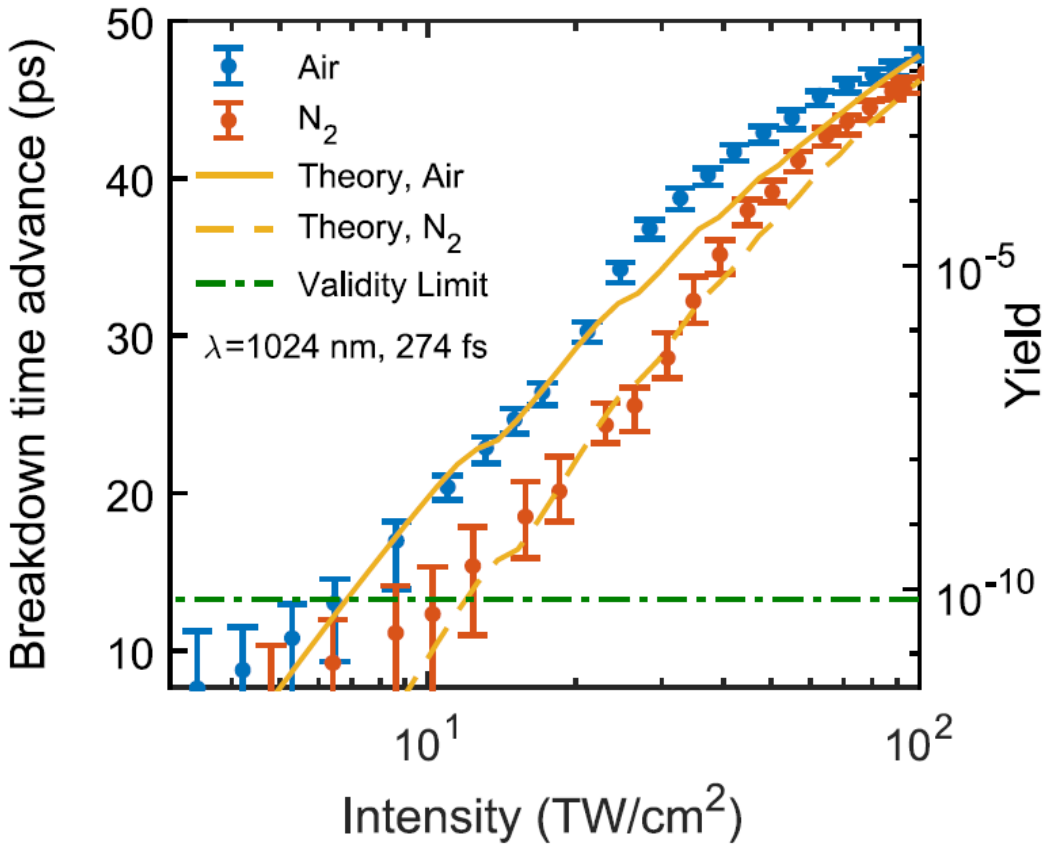

Figure 3.8 Ionization yields measured through breakdown time advance in air (blue) and nitrogen (red). The total ionization yield is calibrated from low intensity measurements using direct counting and experimental data [2] at high intensities. Overlaid in yellow are theoretical ionization curves showing excellent agreement to our data.

3.6 Conclusions

Our results for low-intensity ionization rates are consistent with multiphoton and tunnel ionization of a ubiquitous 6 eV ionization potential contaminant. Despite sensitivity well above the threshold where multi-body effects are predicted to play an important role, our measurements show neither the I^2 dependence, nor the wavelength independence in ionization yield. At higher intensities, this technique shows excellent agreement with theoretical ionization models in both the multiphoton and tunnel regimes up to 100 TW/cm^2.

Taken together, our measurements show an unprecedented measurement of multiphoton and tunnel ionization yields across 14 orders of magnitude. By utilizing the extreme sensitivity of our avalanche breakdown diagnostic and its inherent flexibility to control the probed volume, we have been able to extend plasma density measurements below that of any other technique for small, transient plasmas.

Chapter 4: THz and Low Harmonic Generation from mid-infrared interactions in gases

4.1 Introduction

4.1.1 Two Color THz Generation

Laser-driven generation of THz frequencies requires a symmetry breaking mechanism. The use of optical crystals is one way of achieving this [68–71], taking advantage of their large second-order nonlinearity. Here the generation mechanism is optical rectification with nonlinear susceptibility $\chi^{(2)}(\omega_{THZ}; \omega, -\omega)$. Since most nonlinear crystals cannot easily phase match the conversion from typical optical frequencies to THz frequencies, more complicated schemes using tilted pulse fronts [72–74] or periodic-poled crystals [75–77] have been used to obtain relatively high conversion efficiencies with modest laser intensities. Damage, nonlinear absorption of the laser pulse, material THz absorption, and restrictive phase matching conditions limit the total THz conversion efficiency and bandwidth.

THz generation can also occur in isotropic media such as gases but requires an additional symmetry breaking mechanism. Adding a second co-polarized laser field at the second harmonic achieves this, with the asymmetry controlled by changing the relative phase between the two colors [78,79,88–96,80–87]. The nonlinearity from bound electrons can lead to an effective third order optical rectification with susceptibility $\chi^{(3)}(\omega_{THZ}; 2\omega, -\omega, -\omega)$. Because the third order nonlinearity from neutral gas is extremely small [97,98], intense laser pulses above the ionization threshold can exploit the nonlinearity arising from the bound-free transition for efficient conversion from optical frequencies to THz.

A simple zero-dimensional model can be used to describe how two-color laser fields can generate a transverse plasma current which drives the production of THz frequencies [82–84]. The

electric field of a laser pulse containing both the fundamental and second harmonic frequencies can be expressed by

$$E(t) = E_\omega \cos(\omega t) + E_{2\omega} \cos(2\omega t + \theta)$$

where E_ω and $E_{2\omega}$ are the envelopes of the fundamental and second harmonic and θ is the relative phase between the two colors. Figure 4.1(a) shows the effective field for $\theta = 0$ and $\theta = \pi/2$ over a single optical cycle. For the non-relativistic fields considered here, with normalized vector potential $a_0 = \frac{eE}{mc\omega} \ll 1$, the laser pulse magnetic field can be ignored and free electrons will oscillate with acceleration $\dot{v}(t) = -(e/m_e)E(t)$. In an initially neutral medium with an ionization potential greater than the photon energy, free electrons are the result of nonlinear ionization by the laser field. In this case, the electrons are liberated at some time t' with initial velocity $v(t = t') = 0$. Under the influence of the field the electron velocity will evolve as

$$v(t) = -\frac{e}{m}\int_{t\prime}^{t} E(t)dt$$

This electron transverse electron velocity includes both the oscillations with the laser field and a net drift velocity. The drift velocities as a function of when an electron is liberated is shown in red in Figure 4.1(b). A net motion of electrons will induce a current. To find this current we must consider when electrons are liberated. Using a simple model of multi-photon ionization, described in more detail in Section 1.3 and Chapter 3, the ionization rate can be expressed as $w(t) = I^{38}$, where 38 is the number of λ=3.9 μm ($\varepsilon_\gamma = 0.3$ eV) photons needed to ionize oxygen ($\varepsilon_\gamma = 12.1$ eV) [55]. This rate is shown in blue in Figure 4.1(b), where the highly nonlinear process leads to ionization exclusively near the peak field.

From the ionization rate and electron drift velocity we can calculate the induced transverse plasma current density shown in Figure 4.1(c):

$$\frac{dJ}{dt} \approx ew(t)v(t)$$

We can clearly see that for the symmetric $\theta = 0$ case, the resulting plasma current is an odd function, with zero net transverse current. However, the asymmetry in the $\theta = \pi/2$ field leads to a non-vanishing plasma current. This can be further clarified by looking at a full laser pulse rather than a single cycle. Figure 5.1(d) shows both the electric field (blue curves) and current density (red curves) for a pulse containing about seven optical cycles. By the end of the pulse, the $\theta = 0$ relative phase pulse has no net plasma current, but the non-cancelling drift velocity for $\theta = \pi/2$ pulse leads to a small but non-zero transverse plasma current. This transverse plasma current is responsible for producing the THz frequencies and is polarized along the direction of electron motion, identical to the laser's polarization.

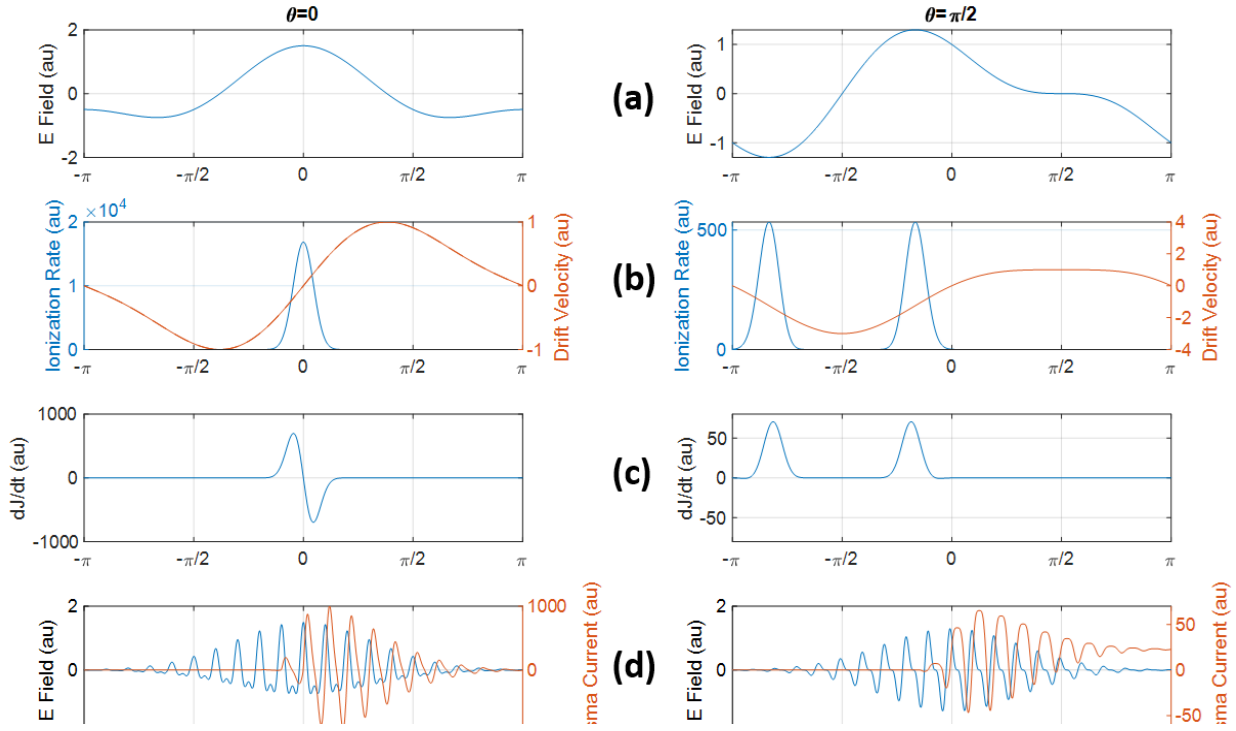

Figure 4.1 Production of transverse plasma currents in two color fields with $\theta = 0$ and $\theta = \pi/2$ relative phase **(a)** Total electric field for a single cycle two-color laser. **(b)** Multiphoton ionization rate, given by $w = I^{38}$ (blue curves) and drift velocity (red curves). **(c)** Plasma current rate induced by driving electrons produced from multiphoton ionization. **(d)** Electric field (blue curves) and net plasma current (red curves) for full laser pulse envelopes.

4.1.2 Low Harmonic Generation

Similar to THz generation, two color laser fields in isotropic media also generate even and odd harmonics. We can first just consider the case of a single color laser field. Below the ionization threshold, harmonics are produced through third harmonic generation governed by the bound electron nonlinearity $\chi^{(3)}(-3\omega;\omega,\omega,\omega)$. Further odd harmonics are generated through cascaded third order frequency mixing processes such as $\chi^{(3)}(-5\omega;3\omega,\omega,\omega)$, $\chi^{(3)}(-5\omega;3\omega,3\omega,-\omega)$, etc. For intensities high enough to drive nonlinear ionization, harmonic generation can also result from the susceptibility associated with the bound-free transition [99]. The strongly driven liberated electrons have a chance of recombining with their parent ion, resulting in emission of high harmonics, typically extending into the extreme ultraviolet [56,100–102].

The bound-free transition nonlinearity arises from the change in plasma frequency as a function of time. During nonlinear ionization, the plasma density ρ increases in a step-wise manner at twice the laser frequency, at both the positive and negative peaks of the laser field. As in Section 4.1.1, the induced plasma current is

$$\frac{dJ}{dt} = \frac{e^2}{m_e}\rho E$$

We can express this in the frequency domain

$$\hat{J} = \frac{ie^2}{m_e\omega}\,\widehat{\rho E}$$

From this we can find the nonlinear polarization from the current

$$\hat{P} = \frac{i}{\omega}\hat{J} = \frac{-e^2}{m_e\omega^2}\widehat{\rho E}$$

The resulting polarization contains terms at all odd harmonics, decreasingly rapidly without plateau. Adding a laser field component at the second harmonic allows the generation of all even

harmonics. The total spectrum includes contributions from the fundamental and its odd harmonics, the second harmonic and its odd harmonics, and frequency mixing between all of these terms. THz generation described in Section 4.1.1 can be thought of as a zeroth order harmonic from this same mechanism.

4.1.3 Mid-Infrared Laser Driven THz and Low Harmonic Generation

Mid-infrared laser sources provide an excellent test bed for measuring the THz and low harmonic generation resulting from nonlinear ionization. As described in Sections 4.1.1 and 4.1.2, nonlinear effects from bound states, bound-free transitions, and free-bound transitions can occur simultaneously. By using a mid-infrared laser, we can exploit the wavelength scaling of these mechanisms to preferentially enhance the nonlinear contribution from the plasma current. The third order nonlinear susceptibility $\chi^{(3)}$ in neutral media exhibits no strong wavelength dependence away from resonances [98,103]. The contribution from the free-bound recollision nonlinearity strongly decreases at longer wavelengths, with both theory and experiments showing harmonic yields scaling with $\sim\lambda^{-(5-6.5)}$ [100,101]. Further, longer wavelength drivers generate higher order harmonics (with cutoff scaling like λ^2), further reducing the effects of the free-bound term on low harmonics.

Conversely, the plasma current driven bound-free nonlinearity relies on the electron quiver velocity, introduced in Section 1.2, which scales linearly with wavelength $v \propto \lambda$. For a fixed intensity, this leads to a predicted scaling of THz and low harmonics with λ^2. Recent experiments have shown THz yield dependence as high as $\lambda^{4.6}$ [88,93–95]. A simple model comparing the bound electron Kerr nonlinearity and the plasma current nonlinearity as a function of laser intensity is shown in Figure 4.2 for both λ=800 nm and 3.9 μm [104]. This model takes the nonlinear susceptibility of nitrogen to be $\chi^{(3)} = 7.9 \times 10^{-20}$ cm^2/W [97,98] and uses a tunneling model for

ionization [82]. The use of longer wavelengths at intensities above the ionization threshold leads to a dominance of the plasma nonlinearity over other effects.

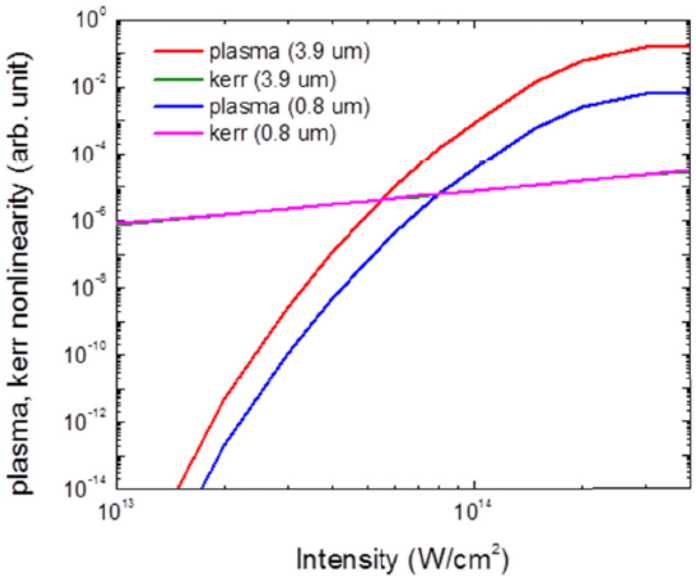

Figure 4.2 Comparison of the contribution from the bound electron Kerr nonlinearity and the plasma current nonlinearity during ionization for λ=800 nm and 3.9 μm lasers. The nonlinearity is approximated by the induced refractive index transient, taken to be representative of third order nonlinearities responsible for the production of low harmonics and THz.

4.2 THz and Low Harmonic Generation in Air

4.2.1 Experimental Outline

As an initial experiment into mid-infrared THz and low harmonic generation, we focused a two-color laser pulse in air and measured the resulting radiation [96]. Figure 4.3(a) shows the schematic layout for this experiment. The laser generates λ=3.9 μm, τ=120 fs pulses in an OPCPA at a 20 Hz repetition rate [32–34]. The beam is focused with a 200 mm focal length CaF_2 lens through a 200 μm thick uncoated z-cut GaSe crystal for second harmonic generation. By tuning the orientation angles α and β, we can tune the crystal for Type 0 SHG, creating a co-polarized two-color field, described further in Section 4.3.1. To prevent damage to the GaSe crystal, the laser

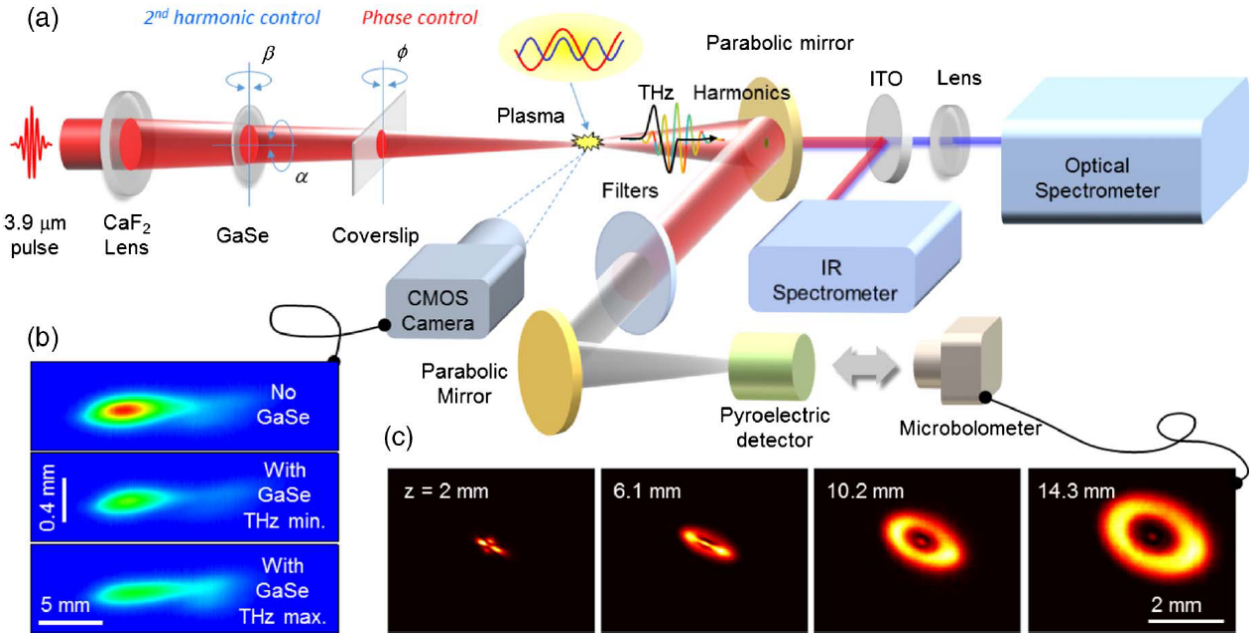

Figure 4.3 Experimental schematic. **(a)** Two-color mid-infrared laser pulses are generated with a GaSe crystal for SHG and a coverslip for relative phase control. When focused into air, a plasma is formed, with the induced plasma current driving low order harmonic and THz generation. The resulting radiation is measured with a ultraviolet-visible spectrometer, and near-infrared spectrometer, and an FTIR with a pyroelectric detector for the THz spectrum. **(b)** visible plasma emission was measured with a CMOS camera to measure the transverse plasma profiles. **(c)** A microbolometer array was used to measure the conical THz radiation profiles as a function of distance from the end of the air plasma.

energy was limited to 5 mJ. A thin coverslip placed at angle ϕ with respect to beam is used to control the relative phase between the fundamental and second harmonic, described more in Section 4.3.2.

The laser is focused to a peak intensity $I = 1.3 \times 10^{14}$ W/cm^2, generating an air plasma at its focus, and producing THz and low-order harmonics. The transverse plasma fluorescence is imaged with a low noise CMOS camera (Thorlabs Quantalux), shown in Figure 4.3(b). After the plasma, the laser is separated with a drilled off-axis parabolic mirror. Most of the optical components of the total field pass through the hole in the mirror. They are further separated with an ITO coated beamsplitter, with the near-infrared portion ($0.95 - 2.5$ μm) collected into a fiber coupled extended InGaAs spectrometer (Avantes NIRLine) and the ultraviolet-visible portion ($200 - 1100$ nm) collected with a lens into a fiber coupled Si spectrometer (Ocean Optics

HR2000+). The low frequency THz components are reflected by the drilled OAP and filtered with pair of calibrated 7 μm longpass filters to remove any residual signals at frequencies greater than 40 THz.

The THz signal is measured with a lithium tantalite pyroelectric detector (Gentec-EO QS9-THz-BL). The spectral response of the detector is relatively flat from optical to THz frequencies and is absolutely calibrated at λ=800 nm and 3.9 μm. A Michelson-type Fourier transform infrared spectrometer is used to characterize the THz spectra and corresponding field autocorrelations. An uncooled microbolometer array (FLIR Tau 2) was used in place of the pyroelectric detector to measure the conical THz radiation profiles as a function of distance from the air plasma, shown in Figure 4.3(c).

4.2.2 Results

The phase dependence on THz generation is a key component of the plasma current generation model. While we cannot directly measure the absolute phase between the fundamental and second harmonic, we can see the effect of the coverslip rotation in both the visible plasma emission and the THz yield.

The transverse plasma profiles measured with the CMOS camera are shown in Figure 4.4(a) and 4.4(b). First, we see an example plasma profile when the coverslip is aligned for maximum THz production. The geometric focus occurs at $z \approx 8$ mm, with Rayleigh length $z_r \approx 8.5$ mm and a 120 μm FWHM spot size. In Figure 4.4(b), we see the plasma profiles, radially integrated, as a function of the initial relative phase θ_0 set by angle-tuning the coverslip. We arbitrarily define $\theta_0 = 0$ as when the coverslip is normal to the laser beam $\phi = 0$. The relative phase as a function of distance can be found by measuring the total plasma fluorescence. Seen in Figure 5.1(b), the ionization rate is maximized when the two colors are in phase and minimized

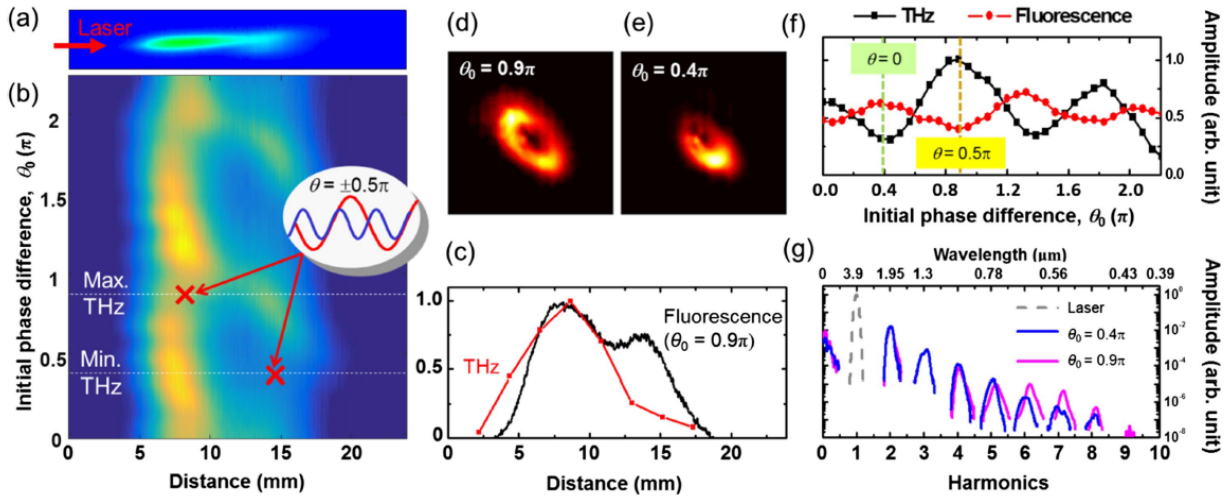

Figure 4.4 Phase dependence ionization and THz generation. **(a)** transverse plasma emission profile when the coverslip is angled to maximize THz production. **(b)** radially integrated plasma profiles as a function of initial relative phase determined by the coverslip angle. $\theta_0 = 0.4\pi$ corresponds to the minimum THz yield and $\theta_0 = 0.9\pi$ corresponds to the THz max. The red X marks show where the absolute relative phase $\theta(\theta_0, z) = \pm 0.5\pi$. **(c)** Local THz emission and plasma fluorescence as a function of axial distance when $\theta_0 = 0.9\pi$. THz beam profiles are measured with a microbolometer for initial relative phase $\theta_0 = 0.4\pi$ **(d)** and $\theta_0 = 0.9\pi$ **(e)**. **(f)** Integrated THz yield and total fluorescence as a function of initial phase difference, showing their $\pi/2$ oscillations and anti-correlation. **(g)** Total harmonic and THz spectra for both $\theta_0 = 0.4\pi$ and $\theta_0 = 0.9\pi$.

when they are out of phase. We can thus identify the fluorescence minima in Figure 4.4(b) as the locations where $\theta(\theta_0, z) = \pm\pi/2$. The fluorescence and THz emission generated when the coverslip is tilted to $\theta_0 = 0.9\pi$ is shown in Figure 4.4(c). An aperture scanning method is used to measure the local THz emission [86]. The THz emission peaks near the laser focus when the relative phase $\theta(\theta_0 = 0.9\pi, z = 8\text{ mm}) \approx \pi/2$. The secondary peak in visible emission at $z \approx 15$ mm is caused by aberrations in the beam focusing, and is also seen in single color plasmas, shown in Figure 4.4(b). This secondary peak is responsible for most of the THz emission when $\theta_0 = 0.4\pi$, in which case plasma dispersion and Guoy phase shifts lead to relative phase $\theta(\theta_0 = 0.4\pi, z = 15\text{ mm}) \approx \pi/2$. Because the laser intensity and ionization are much lower at this position, about 0.8 Rayleigh lengths from the geometric focus, the total THz signal is significantly weaker.

The transverse profiles of the THz radiation is shown in Figure 5.4(d) for $\theta_0 = 0.9\pi$ and Figure 4.4(e) for $\theta_0 = 0.4\pi$. The conical emission pattern pattern is consistent with previous measurements and theoretical predictions [85,87,89] for two-color THz generation. The difference in size observed between the cases is further evidence that changing the initial relative phase affects the position of THz emission.

The phase control over THz and plasma fluorescence is summarized in Figure 4.4(f). Here the plasma emission measured through transverse imaging is summed from $z = 5$ to 10 mm. We see the clear anti-correlation between peaks in THz production and total ionization. Similar phase dependence is seen in the production harmonic, shown in Figure 4.4(g). The spectra shown include measurements from the ultraviolet-visible spectrometer, near-infrared spectrometer, and THz FTIR. The harmonics from 6^{th} to 9^{th} show about an order of magnitude enhancement for $\theta_0 = 0.9\pi$ versus $\theta_0 = 0.4\pi$. While harmonic generation is significantly more complicated, with multiple competing conversion processes happening simultaneously, this shows that harmonic yield from two-color fields can be strongly controlled through relative phase.

Figure 4.5 summarizes our measurements of the THz generation from two-color mid-infrared laser driven plasmas. Field autocorrelations and the corresponding Fourier-transformed spectra are obtained using a Michelson interferometer for both maximum and minimum relative phases, shown in Figure 4.5(a). The spectra are not strongly changed between the two relative phases and peak around 12 THz, with a bandwidth exceeding 30 THz. The dotted line shows the raw measured spectrum, while the solid line shows the spectrum corrected for transmission through the two bandpass filters which significantly distort the lower frequency features due to absorption in the germanium substrate.

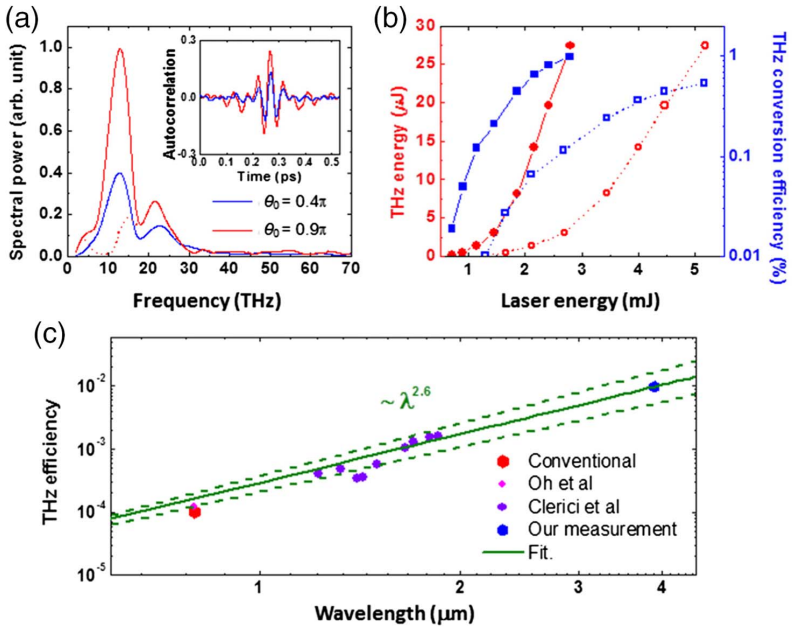

Figure 4.5 (a) THz field autocorrelation and extracted spectra. The dotted line shows the measured spectrum, while the solid lines show the spectra corrected for transmission through two germanium longpass filters. **(b)** THz energy (red) and conversion efficiency (blue) as a function of laser energy. The dotted lines show the energy as measured before the CaF_2 lens while the solid lines include corrections for losses in the GaSe crystal and coverslip. **(c)** Our measured THz conversion efficiency at λ=3.9 μm and previous measurements at λ=0.8-1.8 μm showing a combined $\sim\lambda^{2.6}$ scaling.

The total THz yield and conversion efficiency strongly increase with laser energy, shown in Figure 4.5(b). Again, the dotted lines show the laser energy measured before the CaF_2 lens, while the solid lines are corrected for losses in the uncoated GaSe crystal and coverslip. The maximum conversion produced THz signals of over 25 μJ, corresponding to laser-to-THz conversion efficiencies ~1%. Our ~2% second harmonic conversion (see Section 4.3.1) was relatively low compared to previous experiments generating ~10% at λ=800 nm [89] and ~5% at λ=1.2-1.5 μm [88]. Improving co-polarized second harmonic generation should significantly further increase the field asymmetry and the THz conversion efficiency. Despite not accounting for the differences in second harmonic generation, the wavelength dependent THz efficiency from this experiment and previous experiments [88,89] are shown in Figure 4.5(c). The fit wavelength

dependence $\sim\lambda^{2.6}$ is in good agreement with previous measurements and models for the scaling of THz yield [93,95].

4.2.3 Simulations

In addition to our measurements, we simulated the two-color mixing process with a 2D cylindrically symmetric implementation of the unidirectional pulse propagation equation model [105,106]. The carrier resolved model independently evolves each frequency component, allowing for multi-color fields with wavelength dependent nonlinearities. This model solves a system of ODEs of the form

$$\partial_z A_{k_\perp}(\omega, z) = \frac{i\omega^2}{2\epsilon_0 c^2 k_z^2} e^{-ik_z z} P_{k_\perp}(\omega, z)$$

where the nonlinear polarization term $P_{k_\perp}$ includes the third order nonlinearity from neutral materials [98,103] excluding rotational effects and the plasma nonlinearity term $\hat{P} = \frac{-e^2}{m_e\omega^2}\widehat{\rho E}$ [99]. Ionization is implemented following a strong field model including scaling for laser wavelength and Keldysh parameter [19].

To match our experimental conditions, we generated 120 fs Gaussian pulses with 2.1 mJ in the λ=3.9 μm fundamental and 10.5 μJ (2%) in the second harmonic with controllable relative phase between the two colors. The medium consisted of atmospheric density air comprised of 78% N_2, 21% O_2, and 1% Ar. The simulation window covers 3000 fs with 2^{15} points, encompassing a frequency space from 0.33 THz to 11 PHz. The resulting temporal step size is 0.09 fs, about 70 times smaller than the period of the second harmonic pulse. Frequencies above 1.5 PHz (λ=200 nm) are strongly attenuated corresponding to the UV absorption in air. The transverse spatial grid resolves a 4mm radius space with 400 points. The simulation is solved over 15 cm of propagation with the vacuum focus at z=10 cm and a beam waist of ~100 μm.

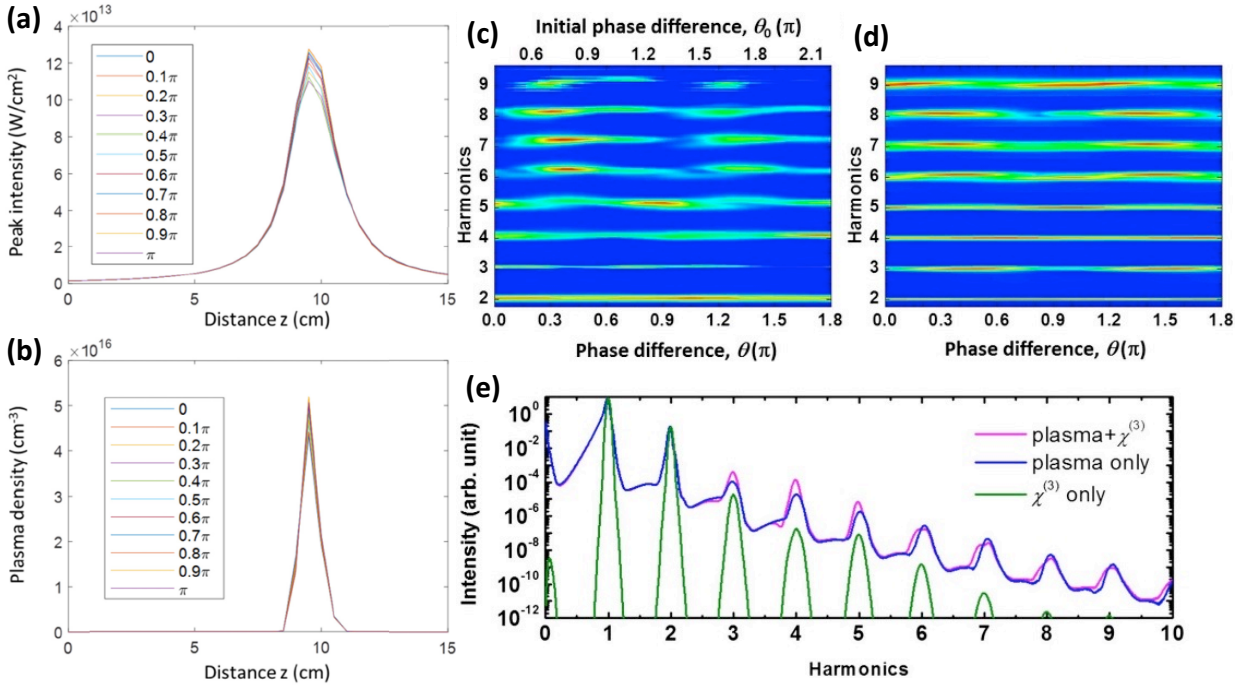

Figure 4.6 Peak intensity **(a)** and plasma density **(b)** from our simulations as a function of distance and relative phase. Comparison between the phase-dependent harmonic generation from measurements **(c)** and simulations **(d)**. **(e)** phase averaged spectra for simulations including only the plasma nonlinearity, only the bound electron nonlinearity, and the combined total nonlinearity.

The peak laser intensity and plasma density depend on the relative phase between the two colors, shown in Figure 4.6(a) and Figure 4.6(b). As seen in the simple 0D model Figure 4.1, the peak intensities and resulting ionization yields are slightly higher for relative phase $\theta = 0$ compared to $\theta = \pi/2$, resulting in peak intensities of $1.1 - 1.3 \times 10^{14}$ TW/cm^2 and plasma densities of $4 - 5 \times 10^{16}$ /cm^3. The phase dependent harmonic yield from our measurements and simulations, shown in Figure 4.6(c) and Figure 4.6(d), display very similar behavior, with the 6th through 9th harmonics anti-correlated to the THz yield with peaks near $\theta = \pi/2$,$3\pi/2$ and the 5th harmonic peaking at $\theta = 0, \pi, 2\pi$. To better understand the physical origin of the harmonic production we performed simulations with the full nonlinearity, only the plasma nonlinearity, and only the bound electron nonlinearity, shown in Figure 4.6(e) averaged over all relatives phases from 0 to π. These results clearly show that THz is almost entirely generated from the plasma current, with the contribution from the bound electrons many orders of

magnitude lower. For the 6th and higher harmonics, the plasma current alone mostly reproduces the total yield, but the bound response slightly alters the shapes, adding a slight broadening on the red side. For the 3rd through 5th harmonics however, even though the bound contribution is several orders of magnitude lower than the plasma contribution, the combined response is significantly different than the plasma alone. While the exact origin of this contribution is hard to isolate, the combination of $\chi^{(3)}$ mixing of plasma-produced harmonics, Kerr self focusing effects on beam propagation, and altered phase matching from both nonlinear source terms can lead to a response significantly greater than the sum of each in isolation [107,108].

4.3 Discussion

4.3.1 Co-polarized Second Harmonic Generation in GaSe

Two-color THz generation requires that both the fundamental and second harmonic laser fields are polarized in the same direction. For second harmonic generation in optical crystals, the polarization dynamics are governed by the relative orientation of the crystal axes with respect to the laser polarization. In general, three generation schemes are possible, corresponding to the phase matching and effective second order nonlinearity for any specific orientation. For Type 0 SHG, two extraordinary-polarized fundamental photons generate an extraordinary-polarized second harmonic photon. For Type 1 SHG, two ordinary-polarized fundamental photons generate an extraordinary-polarized second harmonic photon. For Type II SHG one ordinary and one extraordinary-polarized fundamental photons generate an ordinary polarized second harmonic photon. For Type I and II, a crystal can be chosen such that phase matching conditions are met leading to high conversion efficiencies. However, since the fundamental and second harmonic

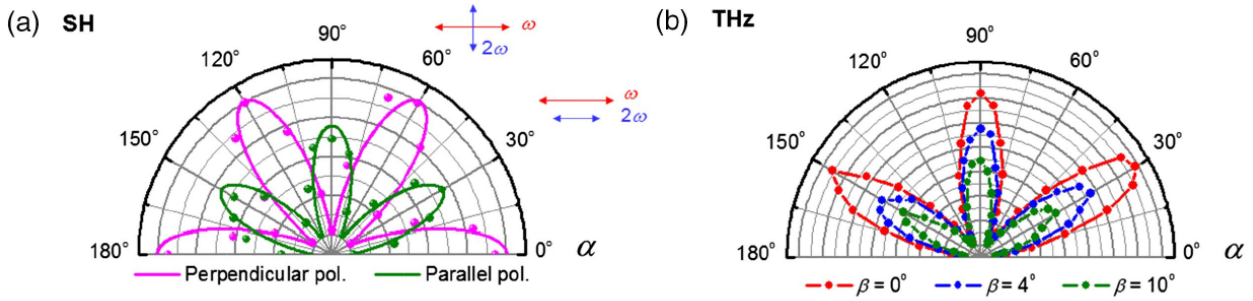

Figure 4.7 (a) Measured second harmonic yield as a function of the crystal rotation about the optical axis, α, which is aligned to the laser axis. Green dots show the measured second harmonic yield with polarization parallel to the fundamental, and the magenta dots show the measurements with perpendicular polarization. Lines show theoretical fit to the data. **(b)** THz production as a function of crystal rotation along the optical axis for laser incidence angles β=0°, 4°, and 10°.

fields are not co-polarized, additional optics are needed to rotate the polarization of the two beams. In the mid-infrared, such optics are not readily-available with high efficiency or damage thresholds, so Type 0 SHG generation must be used to directly produce co-polarized beams.

GaSe is a commonly used nonlinear optical crystal for SHG in the mid-infrared. It has a high second order nonlinearity ($d_{22} \approx 54$ pm/V at λ=10.6 μm) and moderate damage threshold (3 TW/cm^2 for τ=110 ps, λ=2.94 μm pulses) [109]. Due the material structure of GaSe it is only available z-cut, cleaved perpendicular to the optical axis. The index of refraction for ordinary and extraordinary polarizations are n_o=2.72 and n_e=2.40 at λ=3.9 μm and n_o=2.75 and n_e=2.42 at λ=1.95 μm [110]. The high index leads to large Fresnel reflections (about 17% at each face), but the internal absorption is negligible (α<0.1 cm^{-1}) within our 200 μm thick crystal [109], leading 1to about 69% total transmission.

To measure the co-polarized second harmonic yield, we measured the energy ratio between the fundamental and second harmonic using two methods. First, a thin film polarizer with known

transmission and extinction ratio at both the fundamental and second harmonic wavelengths was used to independently measure the horizontal and vertical polarized field components with a power meter. Second, a 10 mm thick uncoated BK7 window was after the GaSe crystal, mostly transmitting the second harmonic and strongly absorbing the fundamental. Using the known absorption and Fresnel losses at both wavelengths allows a distinction between the two colors.

Figure 4.7(a) shows the measured second harmonic yield as a function of the crystal rotation about the optical axis, α. The green dots show the measured second harmonic yield with polarization parallel to the fundamental, and the magenta dots show the measurements with perpendicular polarization. The crystal was oriented such that its optical axis was aligned to the beam axis β=0°. GaSe has a hexagonal crystal structure with $\bar{6}2m$ point group, leading a symmetry in SHG yield when the crystal is rotated 60° about the optical axis [109]. We see both Type 0 and Type 1 SHG, with the expected 60° periodicity, and use the 30° orientation to maximize the Type 0 conversion.

The THz yield is strongly dependent on the energy ratio between the fundamental and co-polarized second harmonic laser components. Figure 4.7(b) shows the measured THz yield as a function of crystal rotation angle α for three crystal tilt angles β=0°, 4°, and 10°. The THz shows the expected peaks when Type 0 SHG is maximized, and the peak signal is found when the laser is incident normal to the crystal face β=0°.

Since Type 0 SHG is not generally a phase matched process, we need to ensure the crystal length is correctly chosen to prevent back-conversion from the second harmonic to the fundamental. Optimum yield for phase-mismatched Type 0 SHG occurs for crystal lengths $L = \frac{N\lambda}{4(n_{2\omega}-n_{\omega})}$ [111], where *N* is an odd-integer. At λ=3.9 μm, the ideal crystal thickness would be 63 μm, but our 200 μm crystal is close to the 190 μm *N*=3 case. At this thickness, the group

velocity walkoff between the fundamental and second harmonic is about 24 fs. While this is a considerable portion of our pulse length, it is mostly compensated by the dispersion in the coverslip used for phase control, discussed in Section 4.3.2.

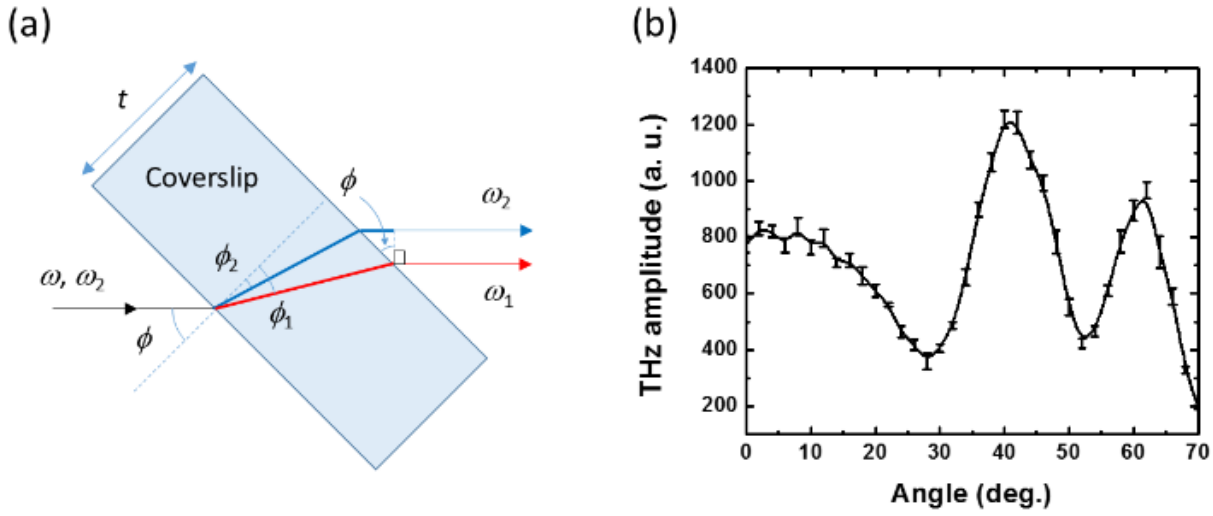

Figure 4.8 (a) Schematic drawing of how the coverslip angle ϕ is used to control the relative phase θ_0 between the two-colors in a laser pulse. **(b)** Total THz yield as a function of coverslip rotation angle.

4.3.2 Relative Phase Control by Coverslip Tilting

As described in Section 4.3.1, controlling the relative phase between the two colors is critical to efficient THz generation. In previous work with near-infrared lasers, the relative phase was controlled using air dispersion [79,83,91,112] or Mach-Zehnder interferometers [92,113]. However, in the mid-infrared, air dispersion is vanishingly small [114] and interferometers require optics not readily available. Instead, a thin coverslip is used to control the relative phase between the two colors, where the tilt angle is controlled to alter the effective thickness [78].

Figure 4.8(a) shows a schematic drawing of how the coverslip angle is used to control the relative phase between the two colors. A t=170±5 μm thick, Schott D263M glass coverslip

(Thorlabs CG15KH1) is placed at angle ϕ with respect to the laser's propagation axis. The two beams are refracted at angles ϕ_1 and ϕ_2, corresponding to the refractive indices at the fundamental and second harmonic: $\phi = \sin^{-1}(\sin\phi\,/n)$. The slight variation in refracted angle corresponds to difference in total path travelled and phase development for the fundamental and second harmonic. The initial relative phase θ_0 between the two colors due to their propagation in the coverslip is given by

$$\theta_0(\phi) = 2\pi t\left\{\frac{n_2}{\lambda_2\cos\phi_2} + \frac{\sin\phi\,(\tan\phi_1 - \tan\phi_2)}{\lambda_2} - \frac{2n_1}{\lambda_1\cos\phi_1}\right\}$$

The measured THz yields as a function of coverslip angle are shown in Figure 5.8(b). For our coverslip, we add about 6π to 9π relative phase between the two pulses as it is rotated between 0° and 70°. The THz generation shows strong oscillations as the initial relative phase goes is incremented by π/2. The transverse spatial offset is about 1 μm, negligible compared to focused beam spots of 50-100 μm for the experiments described in Section 4.2. The temporal walkoff between the two colors is calculated to be about 20 fs when the coverslip is at an angle of $\phi = 42°$, corresponding to the maximum THz yield at initial relative phase $\theta_0 = \pi/2$. This walkoff has the opposite sign of that from the GaSe crystal, so they effectively cancel out. Although the coverslip glass is absorptive at λ=3.9 μm, for a thin uncoated coverslip the losses are predominantly from Fresnel reflections from both surfaces.

Bibliography

1. K. Schuh, J. V. Moloney, and S. W. Koch, "Interaction-induced nonlinear refractive-index reduction of gases in the midinfrared regime," Phys. Rev. E **93**, 1–6 (2016).
2. J. K. Wahlstrand, Y.-H. Cheng, Y.-H. Chen, and H. M. Milchberg, "Optical Nonlinearity in Ar and N 2 near the Ionization Threshold," Phys. Rev. Lett. **107**, 103901 (2011).
3. E. K. Damon and R. G. Tomlinson, "Observation of Ionization of Gases by a Ruby Laser," Appl. Opt. **2**, 546–547 (1963).
4. R. G. Meyerand and A. F. Haught, "Gas Breakdown at Optical Frequencies," Phys. Rev. Lett. **11**, 401–403 (1963).
5. C. DeMichelis, "Laser Induced Gas Breakdown: A Bibliographic Review," IEEE J. Quantum Electron. **5**, 188–202 (1969).
6. J. M. Meek and J. D. Craggs, *Electrical Breakdown of Gases* (Oxford Clarendon Press, 1953).
7. L. Gould and L. W. Roberts, "Breakdown of air at microwave frequencies," J. Appl. Phys. **27**, 1162–1170 (1956).
8. A. D. Macdonald, "High-Frequency Breakdown in Air at High Altitudes," Proc. IRE **47**, 436–441 (1959).
9. E. Yablonovitch, "Similarity principles for laser-induced breakdown in gases," Appl. Phys. Lett. **23**, 121–122 (1973).
10. P. Sprangle, B. Hafizi, H. Milchberg, G. Nusinovich, and A. Zigler, "Active remote detection of radioactivity based on electromagnetic signatures," Phys. Plasmas **21**, (2014).
11. F. V Bunkin and A. M. Prokhorov, "The Excitation and Ionization of Atoms in a Strong Radiation Field," Sov. Phys. JETP **19**, 739–743 (1964).
12. A. Gold and H. B. Bebb, "Theory of Multiphoton Ionization," Phys. Rev. Lett. **14**, 60–63 (1965).
13. L. V. Keldysh, "Ionization in the Field of a Strong Electromagnetic Wave," Sov. Phys. JETP **20**, 1307–1314 (1965).
14. S. Slinker and A. W. Ali, "Electron Momentum Transfer Collision Frequency in N2, O2 and Air," NRL Memo. Rep. (1985).
15. J. Isaacs, C. Miao, and P. Sprangle, "Remote monostatic detection of radioactive material by laser-induced breakdown," Phys. Plasmas **23**, 033507 (2016).
16. J. J. Isaacs, "The Physics of High-Intensity Laser-Matter Interactions and Applications," University of Maryland (2019).
17. D. C. Smith and R. G. Meyerand Jr., "laser Radiation Induced Gas Breakdown," in *Principles of Laser Plasmas*, G. Bekefi, ed. (Wiley-Interscience, 1976), pp. 457–507.
18. J. Way, J. Hummelt, and J. Scharer, "Experimental measurements of multiphoton enhanced air breakdown by a subthreshold intensity excimer laser," J. Appl. Phys. **106**, 083303 (2009).
19. S. V. Popruzhenko, V. D. Mur, V. S. Popov, and D. Bauer, "Strong field ionization rate for arbitrary laser frequencies," Phys. Rev. Lett. **101**, 193003 (2008).
20. A. S. Richardson, *NRL Plasma Formulary* (2019).
21. F. F. Chen, *Introduction to Plasma Physics and Controlled Fusion*, 3rd ed. (Springer, 2016).
22. K. P. Ziock, W. W. Craig, L. Fabris, R. C. Lanza, S. Gallagher, B. K. P. Horn, and N. W.

Madden, "Large area imaging detector for long-range, passive detection of fissile material," IEEE Trans. Nucl. Sci. **51**, 2238–2244 (2004).
23. M. V. Hynes, M. Toolin, B. Harris, J. McElroy, M. S. Wallace, L. J. Schultz, M. Galassi, A. Hoover, M. Mocko, D. Palmer, S. Tornga, D. Wakeford, H. R. Andrews, E. T. H. Clifford, L. Li, N. Bray, D. Locklin, R. Lanza, B. Horn, and D. Wehe, "The Raytheon-SORDS Trimodal Imager," in *Proceedings SPIE 7310, Non-Intrusive Inspection Technologies II* (2009), p. 731003.
24. S. Zelakiewicz, R. Hoctor, A. Ivan, W. Ross, E. Nieters, W. Smith, D. McDevitt, M. Wittbrodt, and B. Milbrath, "SORIS - A standoff radiation imaging system," Nucl. Instruments Methods Phys. Res. A **652**, 5–9 (2011).
25. K. M. Ervin, I. Anusiewicz, P. Skurski, J. Simons, and W. C. Lineberger, "The Only Stable State of O2- Is the X 2∏g Ground State and It (Still!) Has an Adiabatic Electron Detachment Energy of 0.45 eV," J. Phys. Chem. A **107**, 8521–8529 (2003).
26. V. L. Granatstein and G. S. Nusinovich, "Detecting excess ionizing radiation by electromagnetic breakdown of air," J. Appl. Phys. **108**, 063304 (2010).
27. G. S. Nusinovich, "Remote Detection of Concealed Radioactive Materials by Using Focused Powerful Terahertz Radiation," J. Infrared, Millimeter, Terahertz Waves **37**, 515–535 (2016).
28. G. S. Nusinovich, P. Sprangle, C. A. Romero-Talamas, and V. L. Granatstein, "Range, resolution and power of THz systems for remote detection of concealed radioactive materials," J. Appl. Phys. **109**, 083303 (2011).
29. Y. S. Dimant, G. S. Nusinovich, P. Sprangle, J. Penano, C. A. Romero-Talamas, and V. L. Granatstein, "Propagation of gamma rays and production of free electrons in air," J. Appl. Phys. **112**, 083303 (2012).
30. D. Kim, D. Yu, A. Sawant, M. S. Choe, I. Lee, S. G. Kim, and E. Choi, "Remote detection of radioactive material using high-power pulsed electromagnetic radiation," Nat. Commun. **8**, 15394 (2017).
31. R. M. Schwartz, D. Woodbury, J. Isaacs, P. Sprangle, and H. M. Milchberg, "Remote detection of radioactive material using mid-IR laser–driven electron avalanche," Sci. Adv. **5**, eaav6804 (2019).
32. G. Andriukaitis, T. Balčiūnas, S. Ališauskas, A. Pugžlys, A. Baltuška, T. Popmintchev, M.-C. Chen, M. M. Murnane, and H. C. Kapteyn, "90 GW peak power few-cycle mid-infrared pulses from an optical parametric amplifier.," Opt. Lett. **36**, 2755–2757 (2011).
33. A. V Mitrofanov, D. A. Sidorov-Biryukov, A. A. Voronin, A. Pugžlys, G. Andriukaitis, E. a Stepanov, S. Ališauskas, T. Flöri, A. B. Fedotov, V. Y. Panchenko, A. Baltuška, and A. M. Zheltikov, "Subterawatt femtosecond pulses in the mid-infrared range: new spatiotemporal dynamics of high-power electromagnetic fields," Uspekhi Fiz. Nauk **185**, 97–103 (2015).
34. D. C. Woodbury, "Applications of Intense Mid-Infrared Laser-Plasma Interactions," University of Maryland (2020).
35. M. J. Berger, J. S. Coursey, M. A. Zucker, and J. Chang, "Stopping-Power & Range Tables for Electrons, Protons, and Helium Ions," NIST Stand. Ref. Database (n.d.).
36. P. Sprangle, B. Hafizi, H. Milchberg, G. Nusinovich, and A. Zigler, "Active remote detection of radioactivity based on electromagnetic signatures," Phys. Plasmas **21**, 013103 (2014).
37. J. C. Rienstra-Kiracofe, G. S. Tschumper, H. F. Schaefer, S. Nandi, and G. B. Ellison,

"Atomic and molecular electron affinities: Photoelectron experiments and theoretical computations," Chem. Rev. **102**, 231–282 (2002).
38. H. Tawara, N. Ishida, J. Kikuchi, and T. Doke, "Measurements of the W values in argon, nitrogen, and methane for 0.93 to 5.3 MeV alpha particles," Nucl. Instruments Methods Phys. Res. B **29**, 447–455 (1987).
39. D. Woodbury, R. M. Schwartz, and H. M. Milchberg, "Measurement of ultralow radiation-induced charge densities using picosecond mid-IR laser-induced breakdown," Optica **6**, 811 (2019).
40. C. G. Morgan, "Laser-induced breakdown of gases," Reports Prog. Phys. **38**, 621–665 (1975).
41. M. L. Huertas and J. Fontan, "Formation of Stable Positive and Negative Small Ions of Troposhperic Interest," Atmos. Environ. **16**, 2521–2527 (1982).
42. V. A. Mohnen, "Discussion of the formation of major positive and negative ions up to the 50 km level," Pure Appl. Geophys. **84**, 141–151 (1971).
43. D. Woodbury, R. M. Schwartz, E. Rockafellow, J. K. Wahlstrand, and H. M. Milchberg, "Absolute Measurement of Laser Ionization Yield in Atmospheric Pressure Range Gases over 14 Decades," Phys. Rev. Lett. **124**, (2020).
44. P. Polynkin and J. V. Moloney, "Optical breakdown of air triggered by femtosecond laser filaments," Appl. Phys. Lett. **99**, 151103 (2011).
45. V. V Apollonov, L. M. Vasilyak, S. Y. Kazantsev, I. G. Kononov, D. N. Polyakov, A. V Saifulin, and K. N. Firsov, "Electric-discharge guiding by a continuous spark by focusing CO -laser radiation with a conic mirror," Quantum Electron. **32**, 115–120 (2002).
46. K. Mansour, S. M. J, and E. W. Van Stryland, "Nonlinear optical properties of carbon-black suspensions (ink)," J. Opt. Soc. Am. B **9**, 1100–1109 (1992).
47. I. A. Kossyi, A. Y. Kostinsky, A. A. Matveyev, and V. P. Silakov, "Kinetic scheme of the non-equilibrium discharge in nitrogen-oxygen mixtures," Plasma Sources Sci. Technol. **1**, 207–220 (1992).
48. R. F. Fernsler, A. W. Ali, J. R. Graig, and I. M. Vitkovitsky, "The NRL CHMAIR Code: A Disturbed Sea level Air Chemistry Code," NRL Memo. Rep. (1979).
49. A. W. Ali, "Electron Energy Loss Rates in N2, O2, and Air," NRL Memo. Rep. (1984).
50. M. A. Prelas, C. L. Weaver, M. L. Watermann, E. D. Lukosi, R. J. Schott, and D. A. Wisniewski, "A review of nuclear batteries," Prog. Nucl. Energy **75**, 117–148 (2014).
51. M. H. Rees, *Physics and Chemistry of the Upper Atmosphere* (Cambridge University Press, 1989).
52. D. Strickland and G. Mourou, "Compression of amplified chirped optical pulses," Opt. Commun. **55**, 447–449 (1985).
53. S. L. Chin, F. Yergeau, and P. Lavigne, "Tunnel ionisation of Xe in an ultra-intense CO2 laser field (1014 W cm-2) with multiple charge creation," J. Phys. B At. Mol. Opt. Phys. **18**, L213–L215 (1985).
54. S. Augst, D. D. Meyerhofer, D. Strickland, and S. L. Chint, "Laser ionization of noble gases by Coulomb-barrier suppression," J. Opt. Soc. Am. B **8**, 858 (1991).
55. A. Talebpour, J. Yang, and S. L. Chin, "Semi-empirical model for the rate of tunnel ionization of N2 and O2 molecule in an intense Ti:sapphire laser pulse," Opt. Commun. **163**, 29–32 (1999).
56. P. B. Corkum, "Plasma perspective on strong field multiphoton ionization," Phys. Rev. Lett. **71**, 1994–1997 (1993).

57. A. Couairon and A. Mysyrowicz, "Femtosecond filamentation in transparent media," Phys. Rep. **441**, 47–189 (2007).
58. L. Bergé, S. Skupin, R. Nuter, J. Kasparian, and J. P. Wolf, "Ultrashort filaments of light in weakly ionized, optically transparent media," Reports Prog. Phys. **70**, 1633–1713 (2007).
59. K. Schuh, J. Hader, J. V. Moloney, and S. W. Koch, "Influence of many-body interactions during the ionization of gases by short intense optical pulses," Phys. Rev. E **89**, 1–5 (2014).
60. K. Schuh, J. Hader, J. V Moloney, and S. W. Koch, "Influence of optical and interaction-induced dephasing effects on the short-pulse ionization of atomic gases," J. Opt. Soc. Am. B **32**, 1442 (2015).
61. K. Schuh, M. Kolesik, E. M. Wright, J. V. Moloney, and S. W. Koch, "Self-Channeling of High-Power Long-Wave Infrared Pulses in Atomic Gases," Phys. Rev. Lett. **118**, 1–5 (2017).
62. S. Tochitsky, E. Welch, M. Polyanskiy, I. Pogorelsky, P. Panagiotopoulos, M. Kolesik, E. M. Wright, S. W. Koch, J. V. Moloney, J. Pigeon, and C. Joshi, "Megafilament in air formed by self-guided terawatt long-wavelength infrared laser," Nat. Photonics **13**, (2019).
63. A. Sharma, M. N. Slipchenko, M. N. Shneider, X. Wang, K. A. Rahman, and A. Shashurin, "Counting the electrons in a multiphoton ionization by elastic scattering of microwaves," Sci. Rep. **8**, 1–10 (2018).
64. Y.-H. Cheng, J. K. Wahlstrand, N. Jhajj, and H. M. Milchberg, "The effect of long timescale gas dynamics on femtosecond filamentation," Opt. Express **21**, 4740–4751 (2013).
65. S. L. Chin, "Direct experimental evidence of multiphoton ionization of impurities as the initiation process of laser-induced gas breakdown," Can. J. Phys. **48**, 1314–1317 (1970).
66. V. D. Zvorykin, A. O. Levchenko, and N. N. Ustinovskii, "Control of extended high-voltage electric discharges in atmospheric air by UV KrF-laser radiation," Quantum Electron. **41**, 227–233 (2011).
67. J. K. Wahlstrand, S. Zahedpour, A. Bahl, M. Kolesik, and H. M. Milchberg, "Bound-Electron Nonlinearity beyond the Ionization Threshold," Phys. Rev. Lett. **120**, 183901 (2018).
68. X. Wu, S. Carbajo, K. Ravi, F. Ahr, and F. X. Kärtner, "Terahertz generation and its limitations in lithium niobate by optical rectification," Adv. Solid State Lasers, ASSL 2014 **39**, 5403–5406 (2014).
69. M. Jazbinsek, U. Puc, A. Abina, and A. Zidansek, "Organic crystals for THz photonics," Appl. Sci. **9**, 1–44 (2019).
70. K. Reimann, R. P. Smith, A. M. Weiner, T. Elsaesser, and M. Woerner, "Direct field-resolved detection of terahertz transients with amplitudes of megavolts per centimeter," Opt. Lett. **28**, 471 (2003).
71. R. Huber, A. Brodschelm, F. Tauser, and A. Leitenstorfer, "Generation and field-resolved detection of femtosecond electromagnetic pulses tunable up to 41 THz," Appl. Phys. Lett. **76**, 3191–3193 (2000).
72. K. Ravi, W. R. Huang, S. Carbajo, E. A. Nanni, D. N. Schimpf, E. P. Ippen, and F. X. Kärtner, "Theory of terahertz generation by optical rectification using tilted-pulse-fronts," Opt. Express **23**, 5253 (2015).

73. J. Hebling, G. Almasi, I. Kozma, and J. Kuhl, "Velocity matching by pulse front tilting for large area THz-pulse generation," Opt. Express **10**, 1161 (2002).
74. K. L. Yeh, M. C. Hoffmann, J. Hebling, and K. A. Nelson, "Generation of 10 μj ultrashort terahertz pulses by optical rectification," Appl. Phys. Lett. **90**, (2007).
75. R. Chen, G. Sun, G. Xu, Y. J. Ding, and I. B. Zotova, "Generation of high-frequency terahertz waves in periodically poled LiNbO 3 based on backward parametric interaction," Appl. Phys. Lett. **101**, 3–6 (2012).
76. Y. J. Ding and J. B. Khurgin, "A new scheme for efficient generation of coherent and incoherent submillimeter to THz waves in periodically-poled lithium niobate," Opt. Commun. **148**, 105–109 (1998).
77. K. L. Vodopyanov, "Optical THz-wave generation with periodically-inverted GaAs," Laser Photonics Rev. **2**, 11–25 (2008).
78. D. J. Cook and R. M. Hochstrasser, "Intense terahertz pulses by four-wave rectification in air," Opt. Lett. **25**, 1210 (2000).
79. M. Kress, T. Löffler, S. Eden, M. Thomson, and H. G. Roskos, "Terahertz-pulse generation by photoionization of air with laser pulses composed of both fundamental and second-harmonic waves," Opt. Lett. **29**, 1120 (2004).
80. T. Bartel, K. Reimann, M. Woerner, and T. Elsaesser, "Generation of THz transients with high electric-field amplitudes," Opt. Lett. **30**, 2805–2807 (2005).
81. X. Xie, J. Dai, and X. C. Zhang, "Coherent control of THz wave generation in ambient air," Phys. Rev. Lett. **96**, 1–4 (2006).
82. K.-Y. Kim, J. H. Glownia, A. J. Taylor, and G. Rodriguez, "Terahertz emission from ultrafast ionizing air in symmetry-broken laser fields," Opt. Express **15**, 4577 (2007).
83. K. Y. Kim, A. J. Taylor, J. H. Glownia, and G. Rodriguez, "Coherent control of terahertz supercontinuum generation in ultrafast laser-gas interactions," Nat. Photonics **2**, 605–609 (2008).
84. K. Y. Kim, "Generation of coherent terahertz radiation in ultrafast laser-gas interactions," Phys. Plasmas **16**, (2009).
85. Y. S. You, T. I. Oh, and K. Y. Kim, "Off-axis phase-matched terahertz emission from two-color laser-induced plasma filaments," Phys. Rev. Lett. **109**, 1–5 (2012).
86. T. I. Oh, Y. S. You, N. Jhajj, E. W. Rosenthal, H. M. Milchberg, and K. Y. Kim, "Scaling and saturation of high-power terahertz radiation generation in two-color laser filamentation," Appl. Phys. Lett. **102**, (2013).
87. L. A. Johnson, J. P. Palastro, T. M. Antonsen, and K. Y. Kim, "THz generation by optical Cherenkov emission from ionizing two-color laser pulses," Phys. Rev. A **88**, 1–9 (2013).
88. M. Clerici, M. Peccianti, B. E. Schmidt, L. Caspani, M. Shalaby, M. Giguère, A. Lotti, A. Couairon, F. Légaré, T. Ozaki, D. Faccio, and R. Morandotti, "Wavelength scaling of terahertz generation by gas ionization," Phys. Rev. Lett. **110**, 1–5 (2013).
89. T. I. Oh, Y. J. Yoo, Y. S. You, and K. Y. Kim, "Generation of strong terahertz fields exceeding 8 MV/cm at 1kHz and real-time beam profiling," Appl. Phys. Lett. **105**, 1–5 (2014).
90. I. Babushkin, W. Kuehn, C. Köhler, S. Skupin, L. Bergé, K. Reimann, M. Woerner, J. Herrmann, and T. Elsaesser, "Ultrafast spatiotemporal dynamics of terahertz generation by ionizing two-color femtosecond pulses in gases," Phys. Rev. Lett. **105**, 1–4 (2010).
91. H. Wen and A. M. Lindenberg, "Coherent Terahertz Polarization Control through Manipulation of Electron Trajectories," Phys. Rev. Lett. **103**, 2–5 (2009).

92. D. Zhang, Z. Lü, C. Meng, X. Du, Z. Zhou, Z. Zhao, and J. Yuan, "Synchronizing terahertz wave generation with attosecond bursts," Phys. Rev. Lett. **109**, 1–5 (2012).
93. A. Nguyen, P. González de Alaiza Martínez, J. Déchard, I. Thiele, I. Babushkin, S. Skupin, and L. Bergé, "Spectral dynamics of THz pulses generated by two-color laser filaments in air: the role of Kerr nonlinearities and pump wavelength," Opt. Express **25**, 4720 (2017).
94. A. Nguyen, P. González De Alaiza Martínez, I. Thiele, S. Skupin, and L. Bergé, "Broadband terahertz radiation from two-color mid- and far-infrared laser filaments in air," Phys. Rev. A **97**, 3–7 (2018).
95. A. Nguyen, K. J. Kaltenecker, J.-C. Delagnes, B. Zhou, E. Cormier, N. Fedorov, R. Bouillaud, D. Descamps, I. Thiele, S. Skupin, P. U. Jepsen, and L. Bergé, "Wavelength scaling of terahertz pulse energies delivered by two-color air plasmas," Opt. Lett. **44**, 1488 (2019).
96. D. Jang, R. M. Schwartz, D. Woodbury, J. Griff-McMahon, A. H. Younis, H. M. Milchberg, and K.-Y. Kim, "Efficient terahertz and Brunel harmonic generation from air plasma via mid-infrared coherent control," Optica **6**, 1338 (2019).
97. J. K. Wahlstrand, S. Zahedpour, Y.-H. Cheng, J. P. Palastro, and H. M. Milchberg, "Absolute measurement of the ultrafast nonlinear electronic and rovibrational response in H 2 and D 2," Phys. Rev. A **92**, 063828 (2015).
98. S. Zahedpour, S. W. Hancock, and H. M. Milchberg, "Ultrashort infrared 25–11 μm pulses: spatiotemporal profiles and absolute nonlinear response of air constituents," Opt. Lett. **44**, 843 (2019).
99. F. Brunel, "Harmonic generation due to plasma effects in a gas undergoing multiphoton ionization in the high-intensity limit," J. Opt. Soc. Am. B **7**, 521 (1990).
100. A. D. Shiner, C. Trallero-Herrero, N. Kajumba, H. C. Bandulet, D. Comtois, F. Légaré, M. Giguère, J. C. Kieffer, P. B. Corkum, and D. M. Villeneuve, "Wavelength scaling of high harmonic generation efficiency," Phys. Rev. Lett. **103**, 1–4 (2009).
101. J. Tate, T. Auguste, H. G. Muller, P. Salières, P. Agostini, and L. F. Dimauro, "Scaling of wave-packet dynamics in an intense midinfrared Field," Phys. Rev. Lett. **98**, 1–4 (2007).
102. E. E. Serebryannikov and A. M. Zheltikov, "Quantum and semiclassical physics behind ultrafast optical nonlinearity in the midinfrared: The role of ionization dynamics within the field half cycle," Phys. Rev. Lett. **113**, 1–5 (2014).
103. S. Zahedpour, J. K. Wahlstrand, and H. M. Milchberg, "Measurement of the Nonlinear Refractive Index of Air Constituents at Mid-Infrared Wavelengths," Opt. Lett. **40**, 5794–5797 (2015).
104. D. Jang, R. M. R. M. Schwartz, D. Woodbury, J. Griff-mcmahon, A. H. A. H. Younis, H. M. H. M. Milchberg, and K. Kim, "Efficient terahertz and Brunel harmonic generation from air plasma via mid-infrared coherent control," Optica **6**, 1338 (2019).
105. M. Kolesik and J. V. Moloney, "Nonlinear optical pulse propagation simulation: From Maxwell's to unidirectional equations," Phys. Rev. E **70**, 036604 (2004).
106. A. Couairon, E. Brambilla, T. Corti, D. Majus, O. de, and M. Kolesik, "Practitioner's guide to laser pulse propagation models and simulation," Eur. Phys. J. Spec. Top. **199**, 5–76 (2011).
107. U. Sapaev, A. Husakou, and J. Herrmann, "Combined action of the bound-electron nonlinearity and the tunnel-ionization current in low-order harmonic generation in noble gases," Opt. Express **21**, 25582 (2013).

108. T. Balciunas, A. J. Verhoef, A. V. Mitrofanov, G. Fan, E. E. Serebryannikov, M. Y. Ivanov, A. M. Zheltikov, and A. Baltuska, "Optical and THz signatures of sub-cycle tunneling dynamics," Chem. Phys. **414**, 92–99 (2013).
109. G. Dmitriev, G. G. Gurzadyan, and D. N. Nikogosyan, *Handbook of Nonlinear Optical Crystals* (Springer, 1999).
110. K. Kato, F. Tanno, and N. Umemura, "Sellmeier and Thermo-Optic Dispersion Formulas for GaSe," Appl. Opt. **52**, 2325–2328 (2013).
111. R. W. Boyd, *Nonlinear Optics*, 3rd ed. (Elsevier, 2008).
112. K.-Y. Kim, J. H. Glownia, A. J. Taylor, and G. Rodriguez, "Terahertz emission from ultrafast ionizing air in symmetry-broken laser fields," Opt. Express **15**, 4577 (2007).
113. Z. Lü, D. Zhang, C. Meng, X. Du, Z. Zhou, Y. Huang, Z. Zhao, and J. Yuan, "Attosecond synchronization of terahertz wave and high-harmonics," J. Phys. B **46**, (2013).
114. R. J. Mathar, "Refractive index of humid air in the infrared: Model fits," J. Opt. A Pure Appl. Opt. **9**, (2007).